

Groupe d'Annecy
Laboratoire
d'Annecy-le-Vieux de
Physique des Particules

Groupe de Lyon
Ecole Normale
Supérieure de Lyon

HADRONIC PHOTON-PHOTON INTERACTIONS AT HIGH ENERGIES

R.Engel

*Institut für Theoretische Physik, Universität Leipzig, D-04109 Leipzig Germany
and Fachbereich Physik, Universität Siegen, D-57068 Siegen, Germany*

and

J.Ranft

Laboratoire de Physique Théorique ENSLAPP
Groupe d'Annecy: LAPP, Chemin de Bellevue, BP 110,
F-74941 Annecy-le-Vieux Cedex, France.*

Abstract

Photon-photon collisions are investigated in the framework of the two-component Dual Parton Model. The model contains contributions from direct, resolved soft and resolved hard interactions. All free parameters of the model are determined in fits to hadron-hadron and photon-hadron cross section data. The model is shown to agree well to hadron production data from hadron-hadron and photon-hadron collisions. The multiparticle production in hadron-hadron, photon-hadron and photon-photon collisions as predicted by the model is compared. Strong differences are only found as function of the transverse momentum variable. The hadron production in photon-photon collisions at present and future electron-positron colliders is studied using photon spectra according to the equivalent photon approximation, according to beamstrahlung and according to backscattered laser radiation.

ENSLAPP-A-540/95
Siegen SI 95-08
September 1995

*URA 14-36 du CNRS, associée à l'Ecole Normale Supérieure de Lyon et à l'Université de Savoie.

1 Introduction

The photon, in it's high-energy interactions with hadrons, behaves very much like a hadron, however with cross sections reduced strongly against pure hadronic cross sections. Besides this soft hadronic interaction, usually described using the Vector Dominance Model (VDM), the photon has a direct (QED) pointlike interaction with the hadronic constituents and it has the resolved hard interaction between it's hadronic constituents and the hadronic constituents of the target. At moderate energies these hard interactions of the photons do not change significantly the general picture of photon-hadron and photon-photon interactions, this is often forgotten if only the hard part of the photon interaction is discussed. Even at high energies, hadronic interactions of photons are characterized by soft multiparticle production. Since the soft component of hadron production cannot be understood purely on the basis of perturbative QCD, one has to rely on models to calculate the multiparticle final states. The Dual Parton Model (DPM) (a recent review is given in Ref. [1]) has been very successfully describing soft hadronic processes in hadron-hadron collisions. Observations like rapidity plateaus and average transverse momenta rising with energy, KNO scaling violation, transverse momentum-multiplicity correlations and minijets pointed out that soft and hard processes are closely related. These properties were understood within the two-component Dual Parton Model for hadron-hadron interactions by Aurenche et al. [2, 3, 4, 5, 6, 7, 8].

Assuming an universal behavior of soft hadronic interactions, it is possible to extent the Dual Parton Model to hadronic interactions involving photons. First studies of photon-hadron interactions in the framework of the two-component Dual Parton Model were done by Engel [9, 10, 11]. This reaction was studied within other models by various authors, one example is the work by Schuler and Sjöstrand [12, 13].

Here we apply the model described in [9, 11] to the study of hadronic photon-photon interactions. In Section II we give a brief introduction to the Dual Parton Model used to describe photon-hadron and photon-photon collisions, a complete account of the model can be found in [9, 11]. An overview of the model realization in the Monte Carlo event generator PHOJET is given. We study with PHOJET hadron-hadron and photon-hadron collisions and compare to data in Section III. In Section IV we compare the properties of minimum bias hadron production as calculated with PHOJET in hadron-hadron, photon-hadron and photon-photon collisions. In Section V we discuss the properties of hadron production via photon-photon collisions at present and future electron-positron colliders. A Summary is given in Section VI.

2 The event generator PHOJET

The realization of the Dual Parton Model with a hard and a soft component in PHOJET is similar to the event generator DTUJET-93 [2, 8] simulating p - p and p - \bar{p} collisions up to very high energies.

In the following, we restrict our discussion of the model to the basic ideas rather than giving the complete expressions for all the formulae and quantities entering the model. More detailed descriptions of the model are given in [9, 11].

In the model, the dual nature of the photon is taken into account by considering the

physical photon state as a superposition of a "bare photon" and virtual hadronic states having the same quantum numbers $J^{PC} = 1^{--}$ as the photon. Since the properties of the high-mass hadronic fluctuations of the photon are not well known, it is necessary to introduce some approximations for calculations. To keep the model as simple as possible, two generic hadronic states $|q\bar{q}\rangle$ and $|q\bar{q}^*\rangle$ have been introduced to describe the hadronic piece of the photon. The low-mass state $|q\bar{q}\rangle$ corresponds to the superposition of the vector mesons ρ , ω and ϕ and a $\pi^+\pi^-$ background. The state $|q\bar{q}^*\rangle$ is used as an approximation for hadronic states with higher masses (e.g. ρ' , ω' or ρ''). The physical photon reads

$$|\gamma\rangle = \sqrt{Z_3} |\gamma_{\text{bare}}\rangle + |\gamma_{\text{had}}\rangle \quad (1)$$

with

$$Z_3 = 1 - \frac{e^2}{f_{q\bar{q}}^2} - \frac{e^2}{f_{q\bar{q}^*}^2} \quad \text{and} \quad |\gamma_{\text{had}}\rangle = \frac{e}{f_{q\bar{q}}} |q\bar{q}\rangle + \frac{e}{f_{q\bar{q}^*}} |q\bar{q}^*\rangle \quad (2)$$

where e denotes the elementary charge.

The interactions of the hadronic fluctuations are described within the Dual Parton Model in terms of reggeon (\mathcal{IR}) and pomeron (\mathcal{IP}) exchanges. For soft processes, photon-hadron duality is used. The energy-dependence of the reggeon and pomeron amplitude is assumed to be the same for all hadronic processes. Therefore, data on hadron-hadron and photon-hadron cross sections can be used to determine the parameters necessary to describe soft photon-photon interactions. However, one does not expect that this photon-hadron universality holds for processes involving short distances (high transverse momenta). There, long- and short-living fluctuations can contribute.

In order to use the framework of the QCD-improved parton model with lowest order matrix elements [14, 15], the pomeron exchange is artificially subdivided into processes involving only *soft* processes and all the other processes with at least one large momentum transfer (*hard* processes). In the model, soft and hard processes are distinguished by applying a transverse momentum cutoff p_\perp^{cutoff} to the partons. On Born-graph level, for example, the photon-photon cross sections read:

(i) reggeon and pomeron exchange (soft processes only)

$$\begin{aligned} \sigma_{\mathcal{IP}}^{\text{tot}}(s) &= \left(\frac{e^2}{f_{q\bar{q}}^2}\right)^2 g_{\mathcal{IP},q\bar{q}}(0) g_{\mathcal{IP},q\bar{q}}(0) \left(\frac{s}{s_0}\right)^{\Delta_{\mathcal{IP}}} \\ \sigma_{\mathcal{IR}}^{\text{tot}}(s) &= \left(\frac{e^2}{f_{q\bar{q}}^2}\right)^2 g_{\mathcal{IR},q\bar{q}}(0) g_{\mathcal{IR},q\bar{q}}(0) \left(\frac{s}{s_0}\right)^{\Delta_{\mathcal{IR}}} \end{aligned} \quad (3)$$

with $\Delta_{\mathcal{P}} = \alpha_{\mathcal{P}}(0) - 1$ and $\Delta_{\mathcal{R}} = \alpha_{\mathcal{R}}(0) - 1$. Here we denote with $\alpha_{\mathcal{P}}(0)$ ($\alpha_{\mathcal{R}}(0)$) the pomeron (reggeon) intercept, and with $g_{\mathcal{IP},q\bar{q}}$ ($g_{\mathcal{IR},q\bar{q}}$) the couplings of the pomeron (reggeon) to the hadronic $q\bar{q}$ -fluctuations.

(ii) hard resolved photon-photon interaction

$$\sigma_{\text{res}}^{\text{hard}}(s, p_\perp^{\text{cutoff}}) = \int dx_1 dx_2 d\hat{t} \sum_{i,j,k,l} \frac{1}{1 + \delta_{k,l}} f_{\gamma,i}(x_1, Q^2) f_{\gamma,j}(x_2, Q^2) \frac{d\sigma_{i,j \rightarrow k,l}^{\text{QCD}}(\hat{s}, \hat{t})}{d\hat{t}} \Theta(p_\perp - p_\perp^{\text{cutoff}}), \quad (4)$$

where $f_{\gamma,i}(x_1, Q^2)$ is the distribution of the parton i in the photon and the sum includes all possible parton configurations i, j, k, l .

(iii) single direct interactions

$$\sigma_{\text{s-dir}}(s, p_\perp^{\text{cutoff}}) = \int dx d\hat{t} \sum_{i,k,l} f_{\gamma,i}(x, Q^2) \frac{d\sigma_{\gamma,i \rightarrow k,l}^{\text{QCD}}(\hat{s}, \hat{t})}{d\hat{t}} \Theta(p_\perp - p_\perp^{\text{cutoff}}) \quad (5)$$

(iv) double direct interactions

$$\sigma_{\text{d-dir}}(s, p_\perp^{\text{cutoff}}) = \int d\hat{t} \sum_k \frac{d\sigma_{\gamma,\gamma \rightarrow k,\bar{k}}(\hat{s}, \hat{t})}{d\hat{t}} \Theta(p_\perp - p_\perp^{\text{cutoff}}). \quad (6)$$

For simplicity, we have written the cross section formulae only for the low-mass state $|q\bar{q}\rangle$. Similar expressions are used for interactions involving the $|q\bar{q}^\star\rangle$ state. If not explicitly stated, all the calculations have been done using the leading order GRV parton distribution functions for the proton [16] and the photon [17].

Assuming Gaussian distributions in impact parameter space, the amplitudes for the different processes can be calculated from the cross sections given above.

The amplitudes corresponding to the one-pomeron exchange between the hadronic fluctuations are unitarized applying a two-channel eikonal formalism similar to [18, 2]. In impact parameter representation, the eikonalized scattering amplitude for resolved photon interactions has the structure

$$a_{\text{res}}(s, B) = \frac{i}{2} \left(\frac{e^2}{f_{q\bar{q}}^2} \right)^2 \left(1 - e^{-\chi(s, B)} \right) \quad (7)$$

with the eikonal function

$$\chi(s, B) = \chi_S(s, B) + \chi_H(s, B) + \chi_D(s, B) + \chi_C(s, B). \quad (8)$$

Here, $\chi_i(s, B)$ denotes the contributions from the different Born graphs: (S) soft part of the pomeron and reggeon, (H) hard part of the pomeron (D) triple- and loop-pomeron, (C) double-pomeron graphs. To get the photon-photon scattering amplitude, the resolved and the direct amplitude given by perturbative QCD are summed up. The complete expressions will be given in [11].

The probabilities to find a photon in one of the generic hadronic states, the coupling constants to the reggeon and pomeron, and the effective reggeon and pomeron intercepts cannot be determined by basic principles. These quantities are treated as free parameters. It was shown in [9] that it is possible to fix the free parameters by a global fit to proton-proton and photon-proton cross sections and elastic slope parameters. In Fig. 1 we show the model predictions for the inelastic photon-photon cross section (including quasi-elastic vector meson production). The diffractive cross sections of quasi-elastic vector meson production (ρ , ω and ϕ), single diffraction dissociation and double diffraction dissociation are given in Fig. 2. In order to show the strong dependence of the model extrapolations on the parton densities of the photon, the cross sections have been calculated with two different parametrizations of the parton distribution functions.

Once the free parameters are determined, the probabilities for the different final state configurations are calculated from the discontinuity of the elastic photon-photon scattering amplitude (optical theorem). The total discontinuity can be expressed as a sum of graphs with k_c soft pomeron cuts, l_c hard pomeron cuts, m_c triple- or loop-pomeron cuts, and n_c double-pomeron cuts by applying the Abramovski-Gribov-Kancheli cutting rules [19, 20]. In impact parameter space one gets for the inelastic cross section

$$\sigma(k_c, l_c, m_c, n_c, s, B) = \frac{(2\chi_S)^{k_c}}{k_c!} \frac{(2\chi_H)^{l_c}}{l_c!} \frac{(2\chi_D)^{m_c}}{m_c!} \frac{(2\chi_C)^{n_c}}{n_c!} \exp[-2\chi(s, B)] \quad (9)$$

with

$$\int d^2B \sum_{k_c+l_c+m_c+n_c=1}^{\infty} \sigma(k_c, l_c, m_c, n_c, s, B) \approx \sigma_{\text{tot}} - \sigma_{\text{qel}}, \quad (10)$$

where σ_{tot} and σ_{qel} denote the total cross section and the cross section of quasi-elastic vector meson production, respectively. We use here the conventions of [9] treating the triple- and loop-pomeron cross sections (and hence χ_D) as negative quantities. In [2] the negative sign is explicitly written in the cross section formulae (9). Since the triple-, loop-, and double-pomeron graphs are objects involving several pomerons, a further resummation is done [2, 11] to allow for the probability interpretation of Eq. (9).

In the Monte Carlo realization of the model, the different final state configurations are sampled from Eq. (9). For pomeron cuts involving a hard scattering, the complete parton kinematics and flavors/colors are sampled according to the Parton Model using a method similar to [21], extended to direct processes. For pomeron cuts without hard large momentum transfer, the partonic interpretation of the Dual Parton Model is used: photons or mesons are split into a quark-antiquark pair whereas baryons are approximated by a quark-diquark pair. The longitudinal momentum fractions of the partons are given by Regge asymptotics [22, 23, 24, 25]. One obtains for the valence quark (x) and diquark ($1 - x$) distribution inside the proton

$$\rho(x) \sim \frac{1}{\sqrt{x}} (1-x)^{1.5} \quad (11)$$

and for the quark antiquark distribution inside the photon

$$\rho(x) \sim \frac{1}{\sqrt{x(1-x)}}. \quad (12)$$

For multiple interaction events, the sea quark momenta are sampled from a

$$\rho(x) \sim \frac{1}{x} \quad (13)$$

distribution. Note that due to energy-momentum conservation, this distribution is influenced by the x -distributions of the valence partons and asymmetric multiple interaction effects (for example, in photon-proton scattering). This will be discussed in detail elsewhere [26]. The transverse momenta of the soft partons are sampled from the distribution

$$\frac{d^2N_s}{d^2p_{\perp}} \sim \exp(-\beta p_{\perp}). \quad (14)$$

The energy-dependent slope parameter β is calculated from the requirement to have a smooth transition between the transverse momentum distributions of the soft constituents and the hard scattered partons.

For diffraction dissociation or double-pomeron scattering, the parton configurations are generated using the same ideas described above applied to pomeron-photon/hadron/pomeron scattering processes. Hence, a diffractive triple-pomeron or loop-pomeron cut can involve hard scattering subprocesses resulting in a rapidity gap event with jets. According to the kinematics of the triple- or loop-pomeron graphs, the mass of the diffractively dissociating systems is sampled from a $1/M_D^{2\alpha_{P(0)}}$ distribution. The momentum transfer in diffraction is obtained from an exponential distribution with mass-dependent slope (see Ref. [9]). For the parton distributions of the pomeron, the CKMT parametrization with a hard gluonic component [27, 28] is used.

Finally, the fragmentation of the sampled partonic final states is done by forming color neutral strings between the partons according to the color flow. For soft processes, the color flow is approximated using the expansion of QCD for large numbers of colors and flavors. This leads to the two-chain configuration characterizing a cut pomeron (as shown in Fig. 3 (a),(b)) and a one-chain system for a cut reggeon. In hard interactions the color flow is taken from the matrix elements directly [29]. The leading contributions of the matrix elements give a two-chain structure which corresponds to a cut pomeron. For example, a cut of a single hard pomeron graph (hard gluon-gluon scattering) is shown in Fig. 3 (c). This method is also applied to the direct photon interactions.

The chains are fragmented using the Lund fragmentation code JETSET 7.3 [30].

3 Hadron-hadron and photon-hadron collisions with PHOJET

Hadron production in hadron-hadron collisions has been extensively studied within the two-component Dual Parton Model using the DTUJET model [2, 8] in p - p and \bar{p} - p collisions and using the DPMJET-II model [31] in hadron-hadron, hadron-nucleus and nucleus-nucleus collisions. Hadron production in photon-hadron collisions is being studied in detail using the PHOJET model by Engel [10, 11]. We present here only a few comparisons of PHOJET results with hadron-hadron and photon-hadron data in order to illustrate, that the model as formulated in PHOJET is very well able to describe these channels. This is certainly required, if we want to apply the model to photon-photon reactions, where nearly no experimental data are available. For photon-photon collisions we have to rely on the predictive power of the model.

3.1 Hadron-hadron collisions

In Figs. 4 and 5 we compare the transverse momentum distributions and pseudorapidity distributions with the results from collider experiments [32, 33, 34]. The rise of the plateau with the collision energy is understood within the model by one of its most important ingredients: the production of multiple soft interactions and multiple hard interactions (minijets) rises with energy. The transverse momentum distributions as measured at col-

linder energies show besides the soft, exponentially damped, low p_\perp component of hadron production the rise of the perturbative hard component with increasing energy. This becomes more and more important with rising energy for minimum-bias hadron production.

Discussing the changes in hadron production with rising energy, we should indicate, that PHOJET in its present version should not be applied for hadron-hadron, photon-hadron or photon-photon collisions at collision energies beyond $\sqrt{s} = 1$ TeV. One possible way, how to apply a model with minijets in the TeV energy region of future proton-proton supercolliders has been implemented in DTUJET-93 [8]. This could also be done in PHOJET, however photon-hadron or photon-photon collisions in the multi-TeV energy range seem not to be foreseen for the near future.

In Figs. 6 and 7 we compare PHOJET calculations to data on longitudinal distributions in the fragmentation region using the Feynman scaling variable x_F . Feynman x_F -distributions have so far only been measured at fixed target energies, at lab. energies well below 1 TeV. It has been shown elsewhere [31], that the Dual Parton Model shows outside the central region (rise of plateau) and the very forward fragmentation region (where the diffractive component is dominating) a very good Feynman scaling behavior.

The seagull-effect, where one plots the average transverse momentum $\langle p_\perp \rangle$ as function of Feynman x_F , demonstrates clearly, that the distributions in transverse momentum and longitudinal momentum are correlated in a nontrivial way. There is no factorization between the transverse momentum and longitudinal momentum distributions, as it is often assumed in oversimplified models of hadron production. In Fig. 8 we compare the seagull effect calculated with PHOJET to data measured in $p_{lab} = 360$ GeV/c proton-proton collisions [35].

3.2 Photon-hadron collisions

The model for photon-hadron collisions is studied in full detail by Engel [11]. Here we present only some of this material in order to make the present paper self-contained.

In Fig. 9 we compare the transverse momentum distribution of charged hadrons calculated with PHOJET for photon-proton collisions with the photon lab. energy $E_\gamma = 140$ GeV with data from the OMEGA Collaboration [36]. The data were obtained with a tagged photon beam in the energy band 110-170 GeV. The agreement of both distributions is excellent, at the largest p_\perp we see already the influence of direct and resolved hard collisions.

In Figs. 10 and 11 we compare PHOJET results with data from the HERA electron-proton collider [37]. In Fig. 10 we find a very good agreement with the transverse momentum distribution of charged hadrons. If we compare to proton-proton collisions (Fig. 4) we observe, that the influence of hard collisions in photon-proton collisions is more prominent than in proton-proton collisions. In Fig. 11 we find a good agreement of the inclusive charged hadron production cross section as function of the pseudorapidity. We stress, that the data as well as the model show a flat pseudorapidity distribution.

4 Comparison of minimum-bias hadron production in hadron-hadron, photon-hadron and photon-photon collisions

In this Section we compare the model predictions for inelastic hadron production in proton-proton, photon-proton and photon-photon collisions at fixed center-of-mass (CMS) energies \sqrt{s} . This is the usual way to present data on hadron-hadron collisions at colliders or in fixed target experiments. Collisions of quasi-real photons with protons at electron-proton colliders and photon-photon collisions at electron-positron colliders are not at fixed photon-proton or photon-photon energy. We will discuss photon-photon collisions at electron-positron colliders in the next Section. If we consider the three reaction channels at fixed energy, then only in order to find the characteristic differences and similarities between the three types of collisions. Since elastic hadron-hadron collisions usually are excluded studying inclusive secondary distributions, again, in order to find the similarities, we also exclude in the reactions with photons the corresponding quasi-elastic diffractive channel i.e. $\gamma + \gamma \rightarrow V + V$, ($V = \rho, \omega, \phi$) but we include all the other diffractive processes.

We start with the distribution, where the three channels differ most strongly, the transverse momentum distribution $dN/dp_{\perp}dp_{\perp}$, see Fig. 12. The difference is striking. The fraction of hard interactions in minimum bias interactions rises from proton-proton collisions over photon-proton collisions to photon-photon collisions. The reason for this is the direct photon interaction and the fact, that the photon structure function is considerably harder than the proton structure function. In photon-photon collisions it is easy to observe already with moderate statistics hadrons with transverse momenta close to the kinematic limit.

However, these differences in the hard scattering do not strongly influence such average properties of the collision as average multiplicities or even average transverse momenta. This can be seen from Table 1, where we collect some average quantities characterizing nondiffractive proton-proton, proton-photon and photon-photon collisions at CMS energies between 10 and 200 GeV. The total and charged multiplicities at all energies are rather near to each other in all channels. Probably the differences in the multiplicities of newly produced hadrons like π^- and \bar{p} are more significant, we find them at all energies rising from p - p over γ - p to γ - γ collisions. Also the average transverse momenta rise as expected from p - p over γ - p to γ - γ . In Table 1 we give also the number of soft pomerons $\langle n \rangle_{\text{softch.}}$ and the number of hard pomerons $\langle n \rangle_{\text{minijets}}$ contributing in average to the hadronic final state. The numbers given are obtained after kinematical corrections due to energy momentum conservation, not the numbers obtained from the unitarization step (it turns out, especially at low energies, that for kinematical reasons not all sampled pomeron cuts can be generated in the Monte Carlo). At low energy, where the number of minijets is very small, we find the number of cut soft pomerons to be the same in all three channels. The number of cut hard pomerons rises at all energies from p - p over γ - p to γ - γ . We see also, that the numbers of cut soft and cut hard pomerons are correlated, at high energies the number of cut soft pomerons decreases from p - p over γ - p to γ - γ .

In Fig. 13 we compare the longitudinal momentum distributions in the form of $x_r dN/dx_r$

for the three channels. $x_r = (p_{\parallel}/|p_{\parallel}|)2E/\sqrt{s}$ is the so called radial scaling variable, very similar to the Feynman variable $x_F = 2p_{\parallel}/\sqrt{s}$. Significant differences between the three channels are only found in the region near $x_r = 1$ or -1 . The reason is the single diffractive component, which in the p - p and γ - p case leads to the diffractive protons, which are obviously missing in γ - γ collisions.

In Fig. 14 we compare the seagull effect in the three channels. We find due to the direct processes in photon-photon collisions, the rise of $\langle p_{\perp} \rangle$ with rising Feynman x_F is more prominent in photon-photon collisions than in proton-proton collisions. In photon-proton interactions we find backwards, in the proton fragmentation region, agreement with the p - p collision and in forward direction, the photon fragmentation region, agreement with photon-photon collisions.

In Figs. 15 and 16 we plot first logarithmically and then linearly the transverse energy distribution $dE_{\perp}/d\eta$. Roughly, these distributions should be equivalent to the pseudo-rapidity distribution $dN/d\eta$ multiplied with the average transverse energy per particle. We observe characteristic differences, which can be understood from the features already discussed. The transverse energy distribution is wider in photon-photon collisions than in proton-proton collisions. The transverse energy distribution rises at all η from p - p over γ - p to γ - γ . For γ - p the distribution agrees backwards with p - p and forwards with γ - γ .

For p - p or \bar{p} - p collisions the transverse energy distribution at $\eta = 0$ is known from ISR experiments and experiments at the CERN collider. The values calculated with PHOJET agree well with these measurements. At HERA it was found, that practically the same transverse energy at $\eta = 0$ is found like in p - p interactions and in collisions of real or virtual photons with protons [38]. This observation agrees well with our results in Figs. 15 and 16.

Finally in Fig. 17 we plot the transverse energy distributions $dN_{\text{jet}}/dE_{\perp,\text{jet}}$ of jets found in the Monte Carlo events from PHOJET. The jets are searched on hadron level using a cone jet finding algorithm with the cone radius $R=1$. We find again: high $E_{\perp,\text{jet}}$ jets are more prominent in γ - γ collisions.

5 Hadron production in photon-photon collisions at present and future electron-positron colliders

5.1 Photon flux calculation

5.1.1 Bremsstrahlung

The flux of quasi-real photons is calculated using the equivalent photon approximation (improved Weizsäcker-Williams spectrum [39, 40, 41]). Within this approximation the $ep \rightarrow eX$ photoproduction cross section is given by

$$\frac{d\sigma_{ep}}{dy} = f_{\gamma,e}(y) \sigma_{\gamma p}(s, 0) \quad (15)$$

with

$$f_{\gamma,e}(y) = \frac{\alpha_{\text{em}}}{2\pi} \left[\frac{1 + (1 - y)^2}{y} \ln \frac{P_{\max}^2}{P_{\min}^2} - 2m_e^2 y \left(\frac{1}{P_{\min}^2} - \frac{1}{P_{\max}^2} \right) \right]. \quad (16)$$

Here, y and $P^2 = -p_\gamma^2$ denote the energy fraction taken by the photon from the electron and the photon virtuality. α_{em} is the fine structure constant. Taking the kinematic limit $P_{\min,\text{kin}}^2$ as lowest photon virtuality allowed one gets with the electron mass m_e and

$$P_{\min,\text{kin}}^2 = \frac{m_e^2 y^2}{1 - y} \quad (17)$$

the spectrum of quasi-real photons

$$f_{\gamma,e}(y) = \frac{\alpha_{\text{em}}}{2\pi} \left(\frac{1 + (1 - y)^2}{y} \ln \frac{(1 - y) P_{\max}^2}{m_e^2 y^2} - \frac{2(1 - y)}{y} \right). \quad (18)$$

A similar expression holds for $ee \rightarrow ee + X$ scattering involving quasi-real photons only

$$\frac{d^2\sigma_{ep}}{dy_1 dy_2} = f_{\gamma,e}(y_1) f_{\gamma,e}(y_2) \sigma_{\gamma\gamma}(s, 0). \quad (19)$$

5.1.2 Beamstrahlung

In case of Gaussian beams, the effective beamstrahlung spectrum has been estimated by Chen et.al. [42]. The dependence of this spectrum on the particle-bunch parameters can be expressed by the beamstrahlung parameter Y :

$$Y = \frac{5r_e^2 E N_e}{6\alpha_{\text{em}} \sigma_z (\sigma_x + \sigma_y) m_e}. \quad (20)$$

Here, E denotes the beam energy, N_e is the number of electrons or positrons in a bunch, σ_x and σ_y are the transverse bunch dimensions, and $r_e = 2.818 \cdot 10^{-12}$ mm is the classical electron radius. The beamstrahlung spectrum is approximated by [42, 43]

$$\begin{aligned} f_{\gamma,e}^{\text{beam}}(y) &= \frac{\kappa^{1/3}}{\Gamma(1/3)} y^{-2/3} (1 - y)^{-1/3} e^{-\kappa y/(1-y)} \\ &\cdot \left\{ \frac{1-w}{\tilde{g}(y)} \left[1 - \frac{1}{\tilde{g}(y) N_\gamma} (1 - e^{-N_\gamma \tilde{g}(y)}) \right] \right. \\ &\left. + w \left[1 - \frac{1}{N_\gamma} (1 - e^{-N_\gamma}) \right] \right\}, \end{aligned} \quad (21)$$

with

$$\tilde{g}(y) = 1 - \frac{1}{2} (1 - y)^{2/3} \left[1 - y + (1 + y) \sqrt{1 + Y^{2/3}} \right] \quad (22)$$

and $\kappa = 2/(3Y)$, $w = 1/(6\sqrt{\kappa})$. The average number of photons N_γ emitted per electron is given by

$$N_\gamma = \frac{5\alpha_{\text{em}}^2 \sigma_z m_e}{2r_e E} \frac{Y}{\sqrt{1 + Y^{2/3}}}. \quad (23)$$

5.1.3 Photonemission by laser-backscattering

Depending on the polarization of the laser light, various photon spectra can be produced [44, 45, 46]. Here we consider only the case of unpolarized laser radiation. Furthermore, we assume that the laser frequency is chosen to be below the pair-creation threshold at the optimal point. Then, the spectrum of backscattered photons can be written as [43]

$$f_{\gamma,e}^{\text{laser}}(y) = \frac{-0.544 y^3 + 2.17 y^2 - 2.63 y + 1.09}{(1-y)^2} \Theta(0.828 - y). \quad (24)$$

5.2 Hadron production in photon-photon collisions at electron-positron linear colliders

There are at present several projects for electron-positron linear colliders under active study. Here we pick out for our calculations only one of these projects, the TESLA linear collider. Details about the most recent TESLA project were given by Brinkmann [47].

Using the formulae discussed in the last subsection we plot in Fig. 18 the photon spectra according to the equivalent photon approximation, the beamstrahlung spectrum using the bunch parameters [47] as given in the caption of Fig. 18 and a backscattered laser spectrum. The photon virtuality was restricted to $P^2 \leq 0.01 \text{ GeV}^2/\text{c}^2$. In Table 2 we give the average photon-photon energies and the weight factors in μb for the three photon spectra and two energies. From Fig. 18 and Table 2 we see, that the beamstrahlung spectrum of the TESLA project is the softest of the three photon spectra, the backscattered laser spectrum is the hardest.

Of course, in the case of a linear collider we will always have to consider for background problems the superposition of the beamstrahlung spectrum and the equivalent photon spectrum.

A reasonable lowest energy for collisions to be sampled using PHOJET is $\sqrt{s}_{\gamma\gamma} = 5 \text{ GeV}$ (PHOJET would however run without problems even down to $\sqrt{s}_{\gamma\gamma} = 2 \text{ GeV}$). Therefore, for all applications in this and the following subsection we always cut the photon spectra at small y in such a way, that this lower energy cut-off is respected.

In Figs. 19 and 20 we plot the cross sections $\sigma dE_{\perp}/d\eta$ for the transverse energy as function of pseudorapidity and $d\sigma/d\eta$ for the charged hadron production as function of pseudorapidity. It is clearly visible, that the backscattered laser spectrum is rather hard and has the highest weight. The beamstrahlung spectrum and the equivalent photon spectrum are rather comparable, the former has the higher weight, the latter is the harder of these two.

The same differences between the three photon spectra are visible in the cross sections $d\sigma/dp_{\perp}$ for charged hadron production as function of the transverse momentum in Fig. 21 for the 500 GeV TESLA collider.

5.3 Hadron production in photon-photon collisions at the LEP-II electron-positron collider

We use throughout this section an electron-positron energy of $\sqrt{s} = 175 \text{ GeV}$ for the phase II of the LEP collider. Of course here we have only to consider the equivalent photon

spectrum. Assuming anti-tagging of the scattered electrons and positrons we restrict the photon virtuality to satisfy $P^2 \leq 1.75 \text{ GeV}^2/\text{c}^2$.

The average photon-photon energy at LEP-II with the given electron-positron energy will be $\sqrt{s}_{\gamma\gamma} = 25 \text{ GeV}$. In Table 3 we compare some average properties of the LEP-II photon-photon collisions with photon-photon collisions at $\sqrt{s}_{\gamma\gamma} = 25 \text{ GeV}$. We find, that the average properties are rather well represented by photon-photon collisions at $\sqrt{s} = 25 \text{ GeV}$.

In the following we consider a calorimeter detector with the pseudorapidity coverage $|\eta| \leq 2.1$. Applying a jet finding algorithm to this detector we can identify jets in the pseudorapidity range $|\eta_{\text{jet}}| \leq 1.1$. For the jets we use generally a lower jet transverse energy cutoff $E_{\perp\text{jet}} \geq 5 \text{ GeV}$.

In Fig. 22 we give the jet transverse energy distribution in the acceptance region given above together with its decomposition into the different hard interaction mechanisms. The single resolved (equal to the single direct) contribution within the acceptance region is surprisingly small. At small $E_{\perp\text{jet}}$ the two resolved contribution dominates, at large $E_{\perp\text{jet}}$ the direct contribution dominates.

To study the influence of multiple soft and multiple hard interactions in the model we plot in Fig. 23 the jet E_{\perp} cross section together with further curves, where multiple soft or multiple hard contributions or both are rejected. The arbitrary threshold between soft and hard partons in the model is $p_{\perp}^{\text{cutoff}} = 3 \text{ GeV}/\text{c}$. The multiple soft, one hard curve coincides nearly with the total $E_{\perp\text{jet}}$ distribution. With the average numbers of minijets given in Table 3 the chance to have more than one minijet in one event is small. This is different for the multiple soft interactions, with an average (see Table 3) around 1.36 soft interactions per event, the chance to have multiple soft chains is rather high.

To study the influence of an upper visible energy cut we plot in Fig. 24 the jet transverse energy cross section together with the distribution obtained with the cut $E_{\text{visible}} \leq 50 \text{ GeV}$ within the acceptance region $|\eta| \leq 2.1$. The 50 GeV cut serves to suppress jets coming from Z^0 decay. For jets with transverse energies below 10 GeV this cut does not change the $E_{\perp\text{jet}}$ distribution drastically. The same is found studying pseudorapidity jet profiles with and without the visible energy cut in Fig. 25. Note that the jets become more narrow with rising energy and also the pedestal under the jets rises with rising jet transverse energy. This again is an effect mainly due to the multiple soft and hard chains.

Finally, in Fig. 26 we plot the cross section as function of the visible energy within the acceptance region. Since we want to search jets with a $E_{\perp\text{jet}} \geq 5 \text{ GeV}$ cutoff, we use a lower threshold for the photon-photon energy $\sqrt{s}_{\gamma\gamma} = 10 \text{ GeV}$. The plot gives the visible energy distribution without restrictions and in a second curve the visible energy obtained if we demand at least one jet with $E_{\perp\text{jet}} \geq 5 \text{ GeV}$ and impose the visible energy cut $E_{\text{visible}} \leq 50 \text{ GeV}$ within the acceptance region given above. We observe: nearly each event with a visible energy above 30 GeV contains at least one jet with $E_{\perp\text{jet}} \geq 5 \text{ GeV}$.

6 Conclusions and summary

The PHOJET model can be used to calculate hadronic events in hadron-hadron, photon-hadron and photon-photon collisions. The model is found to agree well with data in

hadron-hadron and photon-hadron collisions, the predictions for photon-photon collisions do not need any new parameters.

Multiple soft and multiple hard interactions (minijets) lead to a rise of the rapidity plateau, which agrees in hadron-hadron and photon-hadron collisions very well with the rise of the plateau observed experimentally.

Minimum bias hadron production in hadron-hadron, photon-hadron and photon-photon collisions of the same CMS energy is remarkably similar. To see this, one has to restrict the comparison to inelastic events and to exclude also the diffractively produced vector mesons in reactions involving photons. The only striking differences appear in the transverse momentum distribution or distributions, where the transverse momentum behavior is essential. This difference can be understood to be due to the direct photon interaction contribution and due to the photon structure function being considerably harder than hadronic structure functions.

PHOJET can be applied also to photon-photon interactions in electron-hadron and electron-electron or electron-positron colliders. Photon spectra according to the equivalent photon approximation, according to beamstrahlung spectra and backscattered laser radiation in linear electron-positron colliders are implemented at present. It is easy to implement other similar photon spectra. With these possibilities PHOJET should be a tool suitable to study the photon-photon background to other interesting reactions at such colliders.

Acknowledgements

The authors are grateful to P. Aurenche for many helpful discussions and suggestions. They acknowledge the hospitality and support by LAPP, Annecy-le-Vieux, most of the results presented were obtained during stays at LAPP and they acknowledge the invitations to sessions of LEP-II and linear collider study groups by the conveners of these studies. One of the authors (R.E.) was supported by the Deutsche Forschungsgemeinschaft under contract No. Schi 422/1-2.

References

- [1] A. Capella, U. Sukhatme, Chung I Tan and J. Tran Thanh Van: Phys. Rep. **236**, 225 (1994).
- [2] P. Aurenche, F. W. Bopp, A. Capella, J. Kwiecinski, M. Maire, J. Ranft and J. Tran Thanh Van: Phys. Rev. D **45**, 92 (1992).
- [3] A. Capella, J. Tran Thanh Van and J. Kwiecinski: Phys. Rev. Lett. **58**, 2015 (1987).
- [4] F. W. Bopp, A. Capella, J. Ranft and J. Tran Thanh Van: Z. Phys. C **51**, 99 (1991).
- [5] F. W. Bopp, D. Pertermann and J. Ranft: Z. Phys. C **54**, 683 (1992).
- [6] R. Engel, F. W. Bopp, D. Pertermann and J. Ranft: Phys. Rev. D **46**, 5192 (1992).
- [7] S. Roesler, R. Engel and J. Ranft: Z. Phys. C **59**, 481 (1993).
- [8] F. W. Bopp, D. Pertermann, R. Engel and J. Ranft: Phys. Rev. D **49**, 3236 (1994).
- [9] R. Engel: Z. Phys. C **66**, 203 (1995).
- [10] R. Engel: Photoproduction within the Dual Parton Model, Talk given at XXIXth Rencontre de Moriond, in Proceedings of the XXIXth Rencontre de Moriond, Meribel, France, Page 321, ed. by J. Tran Thanh Van, Edition Frontieres, Gif-sur-Yvette, 1994.
- [11] R. Engel: to be published.
- [12] G. A. Schuler and T. Sjöstrand: Nucl. Phys. B **407**, 539 (1993).
- [13] G.A. Schuler and T. Sjöstrand: Phys. Rev. D **49**, 2257 (1994).
- [14] B. L. Combridge, J. Kripfganz and J. Ranft: Phys. Lett. **70B**, 234 (1977).
- [15] D. W. Duke and J. F. Owens: Phys. Rev. D **26**, 1600 (1982).
- [16] M. Glück, E. Reya and A. Vogt: Phys. Rev. D **45**, 3986 (1992).
- [17] M. Glück, E. Reya and A. Vogt: Phys. Rev. D **46**, 1973 (1992).
- [18] A. Capella, J. Kaplan and J. Tran Thanh Van: Nucl. Phys. B **105**, 333 (1976).
- [19] V. A. Abramovski, V. N. Gribov and O. V. Kancheli: Yad. Fis. **18**, 595 (1973).
- [20] K. A. Ter-Martirosyan: Phys. Lett. B **44**, 377 (1973).
- [21] K. Hahn and J. Ranft: Phys. Rev. D **41**, 1463 (1990).
- [22] A. Capella, U. Sukhatme and J. Tran Thanh Van: Z. Phys. C **3**, 329 (1980).
- [23] A. Capella, U. Sukhatme, C. I. Tan and J. Tran Thanh Van: Z. Phys. C **10**, 249 (1980).

- [24] A. B. Kaidalov: Phys. Lett. **116B**, 459 (1982).
- [25] A. B. Kaidalov and K. A. Ter-Martirosyan: Phys. Lett. **117B**, 247 (1982).
- [26] F. W. Bopp and R. Engel: Effects of unitarity corrections in deep inelastic scattering at HERA, Siegen University SI 95-05, 1995.
- [27] A. Capella, A. Kaidalov, C. Merino and J. Tran Thanh Van: Phys. Lett. B **343**, 403 (1995).
- [28] R. Engel, J. Ranft and S. Roesler: Phys. Rev. D **52**, 1459 (1995).
- [29] H. U. Bengtsson: Comp. Phys. Commun. **31**, 323 (1984).
- [30] H. U. Bengtsson and T. Sjöstrand: Comput. Phys. Commun. **46**, 43 (1987).
- [31] J. Ranft: Phys. Rev. D **51**, 64 (1995).
- [32] C. Albajar et al.: Nucl. Phys. B **335**, 261 (1990).
- [33] G. J. Alner et al.: Z. Phys. C **33**, 1 (1986).
- [34] F. Abe et al.: Phys. Rev. D **41**, 2330 (1990).
- [35] EHS-RCBC Collaboration: J. L. Bailly et al.: Z. Phys. C **35**, 295 (1987).
- [36] OMEGA Photon Collab.: R. J. Apsimon et al.: Z. Phys. C **43**, 63 (1989).
- [37] H1 Collab.: I. Abt et al.: Phys. Lett. B **328**, 177 (1994).
- [38] H1 Collab.: S. Aid et al.: Comparison of Deep Inelastic Scattering with Photoproduction at HERA, DESY 95-156, 1995.
- [39] C. F. von Weizsäcker: Z. Phys. **88**, 612 (1934).
- [40] E. J. Williams: Phys. Rev. **45**, 729 (1934).
- [41] S. Frixione, M. Mangano, P. Nason and G. Ridolfi: Phys. Lett. B **319**, 339 (1993).
- [42] P. Chen, T. L. Barklow and M. E. Peskin: Phys. Rev. D **49**, 3209 (1994).
- [43] M. Drees and R. M. Godbole: Z. Phys. C **59**, 591 (1993).
- [44] I. F. Ginzburg, G. L. Kotkin, V. G. Serbo and V. I. Telnov: Nucl. Instrum. Methods **205**, 47 (1983).
- [45] I. F. Ginzburg, G. L. Kotkin, V. G. Serbo and V. I. Telnov: Nucl. Instrum. Methods **219**, 5 (1984).
- [46] V. I. Telnov: Nucl. Instrum. Methods **294**, 72 (1990).
- [47] R. Brinkmann: SBLC and TESLA general design overview, Presentation at the Linear Collider workshop, Gran Sasso, Italy, 1995.

- [48] PLUTO Collab.: M. Feindt et al.: Talk given at 7th International Workshop on photon-photon interactions, Paris, 1986.
- [49] TPC/2 γ Collab.: H. Aihara et al.: Phys. Rev. D **41**, 2667 (1990).
- [50] CELLO Collab.: H. J. Behrend et al.: Z. Phys. C **51**, 365 (1991).
- [51] PLUTO Collab.: C. Berger et al.: Phys. Lett. **149B**, 421 (1984).
- [52] D. Bintinger et al.: Phys. Rev. Lett. **54**, 763 (1985).
- [53] G. A. Schuler and T. Sjöstrand: Low- and high-mass components of the photon distribution functions, CERN-TH/95-62, 1994.
- [54] G. A. Schuler and T. Sjöstrand: Preprint CERN-TH.7193/94, presented at the Workshop on Two Photon Physics, Paris (1994).
- [55] T. Kafka et al.: Phys. Rev. D **16**, 1261 (1977).
- [56] A. E. Brenner et al.: Phys. Rev. D **26**, 1497 (1982).
- [57] LEBS-EHS Collaboration: M. Aguilar-Benitez et al.: Z. Phys. C **50**, 405 (1991).
- [58] EHS-RCBC Collaboration: J. L. Bailly et al.: Z. Phys. C **35**, 309 (1987).

Table 1 Comparison of average quantities characterizing hadron production in non-diffractive $p-p$, $\gamma-p$ and $\gamma-\gamma$ collisions at cms energies between 10 and 200 GeV. All average transverse momenta are given in GeV/c.

\sqrt{s}	Quantity	$p-p$	$\gamma-p$	$\gamma-\gamma$
10	n_{tot}	11.2	11.1	11.7
10	n_{ch}	6.65	6.53	6.86
10	n_{π^-}	2.17	2.44	2.88
10	$n_{\bar{p}}$	0.027	0.063	0.11
10	$\langle p_{\perp ch} \rangle_{centr.\eta}$	0.39	0.38	0.42
10	$\langle p_{\perp} \rangle_{\pi^-}$	0.32	0.33	0.36
10	$\langle p_{\perp} \rangle_{\bar{p}}$	0.41	0.43	0.47
10	$\langle n \rangle_{softch.}$	1.16	1.19	1.22
10	$\langle n \rangle_{minijets}$	0.	0.00004	0.0020
20	n_{tot}	16.4	16.6	17.1
20	n_{ch}	9.64	9.71	10.00
20	n_{π^-}	3.44	3.78	4.18
20	$n_{\bar{p}}$	0.086	0.14	0.20
20	$\langle p_{\perp ch} \rangle_{centr.\eta}$	0.37	0.38	0.44
20	$\langle p_{\perp} \rangle_{\pi^-}$	0.32	0.34	0.38
20	$\langle p_{\perp} \rangle_{\bar{p}}$	0.42	0.45	0.52
20	$\langle n \rangle_{softch.}$	1.26	1.33	1.31
20	$\langle n \rangle_{minijets}$	0.0003	0.0025	0.028
50	n_{tot}	24.8	26.5	26.9
50	n_{ch}	14.5	15.5	15.6
50	n_{π^-}	5.49	6.19	6.53
50	$n_{\bar{p}}$	0.21	0.27	0.34

Continuation of Table 1

\sqrt{s}	Quantity	$p-p$	$\gamma-p$	$\gamma-\gamma$
50	$< p_{\perp ch} >_{centr.\eta}$	0.38	0.40	0.46
50	$< p_{\perp} >_{\pi^-}$	0.33	0.35	0.40
50	$< p_{\perp} >_{\bar{p}}$	0.44	0.47	0.57
50	$< n >_{softch.}$	1.50	1.68	1.44
50	$< n >_{minijets}$	0.0096	0.035	0.17
200	n_{tot}	40.1	46.2	47.5
200	n_{ch}	23.3	26.9	27.6
200	n_{π^-}	9.16	10.94	11.46
200	$n_{\bar{p}}$	0.46	0.59	0.67
200	$< p_{\perp ch} >_{centr.\eta}$	0.40	0.42	0.48
200	$< p_{\perp} >_{\pi^-}$	0.35	0.38	0.42
200	$< p_{\perp} >_{\bar{p}}$	0.47	0.53	0.64
200	$< n >_{softch.}$	1.59	1.87	1.29
200	$< n >_{minijets}$	0.17	0.36	1.01

Table 2 Average photon–photon energies and weight factors in μb for the three photon spectra and two linear collider energies.

\sqrt{s}	Photon spectrum	$\sqrt{s}_{\gamma\gamma}$	Weight (μb)
500	W.–W.	50	0.0067
500	Beamst.	16.7	0.038
500	B.Laser	252	0.47
1000	W.–W.	105	0.0075
1000	Beamst.	41	0.026
1000	B.Laser	509	0.59

Table 3 Comparison of average quantities for LEP-II photon–photon collisions with photon–photon collisions at $\sqrt{s}_{\gamma\gamma} = 25$ GeV.

Quantity	LEP-II $\gamma\gamma$	$\gamma\gamma$ at 25 GeV
n_{tot}	15.6	17.2
n_{ch}	9.19	10.1
n_{π^+}	3.74	4.12
n_{π^-}	3.74	4.12
$n_{\bar{p}}$	0.17	0.19
$\langle p_\perp \rangle_{\pi^-}$	0.37	0.37
$\langle p_\perp \rangle_{\bar{p}}$	0.50	0.50
$\langle n \rangle_{softch.}$	1.36	1.44
$\langle n \rangle_{minijets}$	0.035	0.028
Weight (μb)	0.0032	

Figure 1: Inelastic photon-photon cross sections as calculated in the model compared with experimental data at low energies [48, 49, 50, 51, 52]. The two curves from the model were calculated using the GRV LO photon structure function [17] and the SaS 2M photon structure function [53]. The differences between both curves at high energy demonstrate the uncertainties of the predictions due to the limited data available on the photon structure function. Our curve calculated with the SaS 2M structure function agrees practically with the cross section calculated with the same structure function but using another model by Schuler and Sjöstrand [54].

Figure 2: Diffractive cross sections as calculated with PHOJET using the GRV LO photon structure function [17] and the SaS 2M photon structure function [53]. The upper curve is for each of the three cross sections the one obtained with the GRV LO structure function.

Figure 3: Unitarity cut of a one-pomeron graph: the unitarity sum including all possible final states is subdivided into final states with low- p_\perp partons and into final states with at least one parton satisfying $p_\perp \geq p_\perp^{\text{cutoff}}$.

Figure 4: Comparison of transverse momentum distributions of charged hadrons with collider data at $\sqrt{s} = 200$ GeV [32]. The calculation uses the Dual Parton Model code PHOJET.

Figure 5: Pseudorapidity distributions of charged hadrons produced in \bar{p} - p collisions as calculated with PHOJET are compared to collider data from the UA-5 Collaboration [33, 34] for the energy $\sqrt{s} = 200$ GeV.

Figure 6: Comparison of Feynman x_F distributions of π^+ -mesons produced in proton-proton collisions at 205 and 175 GeV. The experimental data are from Kafka et al. [55] and from Brenner et al. [56]. The data from both experiments agree rather well with each other. The calculation uses the Dual Parton Model PHOJET.

Figure 7: Comparison of Feynman x_F distributions of π^- -mesons produced in proton-proton collisions at 400 and 360 GeV. The experimental data are from the Aguilar-Benitez et al. [57] and from the EHS-RCBC Collaboration [58]. The data from both experiments agree rather well with each other, in fact most of the data points of [58] are below the [57] data. The calculation uses the Dual Parton Model PHOJET.

Figure 8: Comparison of the seagull effect in the reaction $p+p \rightarrow h^- + X$ at 360 GeV. The data are from the EHS-RCBC Collaboration [35]. The calculation uses the Dual Parton Model PHOJET.

Figure 9: Comparison of the transverse momentum distribution of charged hadrons with $0 \leq x_F \leq 1$ as calculated with PHOJET at the average photon energy of 140 GeV with data. The data are from the OMEGA Collaboration [36] measured with a tagged photon beam in the energy band 110-170 GeV.

Figure 10: Comparison of the transverse momentum distribution of charged hadrons produced by quasi-real photons in electron-proton collisions at HERA [37] with the PHOJET calculation [10]. The data and the calculation is in the pseudorapidity region $-1.5 \leq \eta_{\text{lab}} \leq 1.5$.

Figure 11: Comparison of the inclusive pseudorapidity cross section of charged hadrons produced by quasi-real photons in electron-proton collisions at HERA [37] with the PHOJET calculation [10].

Figure 12: We compare at the collision energy $\sqrt{s} = 200$ GeV the transverse momentum distribution in invariant form for all charged hadrons produced in proton-proton, photon-proton and photon-photon collisions. The calculation was done with PHOJET for inelastic collisions, excluding in photon-proton collisions the $V-p$ and in photon-photon collisions the $V-V$ diffractive production of vector mesons $V = \rho, \omega$ and ϕ .

Figure 13: We compare at the collision energy $\sqrt{s} = 200$ GeV the radial $x_r = 2E/\sqrt{s}$ distribution in invariant form for all charged hadrons produced in proton-proton, photon-proton and photon-photon collisions. The calculation was done with PHOJET for inelastic collisions, excluding in photon-proton collisions the $V-p$ and in photon-photon collisions the $V-V$ diffractive contributions.

Figure 14: We compare at the collision energy $\sqrt{s} = 200$ GeV the average transverse momentum of charged hadrons produced in proton-proton, photon-proton and photon-photon collisions as function of the Feynman x_F variable (seagull effect). The calculation was done with PHOJET for inelastic collisions, excluding in photon-proton collisions the $V-p$ and in photon-photon collisions the $V-V$ diffractive contributions.

Figure 15: We compare at the collision energies $\sqrt{s} = 20$ GeV and 200 GeV in a log-plot the distribution of the transverse energy E_{\perp} as function of the pseudorapidity η for proton-proton, photon-proton and photon-photon collisions. The calculation was done with PHOJET for inelastic collisions, excluding in photon-proton collisions the V - p and in photon-photon collisions the V - V diffractive contributions.

Figure 16: We compare at the collision energies $\sqrt{s} = 20$ GeV, 200 GeV and 1000 GeV in a linear plot the distribution of the transverse energy E_{\perp} as function of the pseudorapidity η for proton-proton, photon-proton and photon-photon collisions. The calculation was done with PHOJET for inelastic collisions, excluding in photon-proton collisions the V - p and in photon-photon collisions the V - V diffractive contributions.

Figure 17: We compare at the collision energy $\sqrt{s} = 200$ GeV the transverse energy distribution for hadronic jets (identified using a jet-finding algorithm) produced in proton-proton, photon-proton and photon-photon collisions. The calculation was done with PHOJET.

Figure 18: Photon fluxes at a $\sqrt{s} = 500$ GeV linear collider TESLA [47]. Given are the improved Weizsäcker-Williams spectrum, the beamstrahlung spectrum using the bunch parameters $N_e = 1.8 \cdot 10^{10}$, $\sigma_x = 598$ nm, $\sigma_y = 6.5$ nm and $\sigma_z = 0.5$ mm [47], and a backscattered laser spectrum.

Figure 19: Cross section weighted transverse energy distributions $\sigma dE_{\perp}/d\eta$ measured in μb GeV at the $\sqrt{s} = 500$ and 1000 GeV TESLA linear colliders [47]. Given are the distributions for the Weizsäcker-Williams photon spectrum, the beamstrahlung spectrum and a backscattered laser spectrum.

Figure 20: Pseudorapidity cross sections $d\sigma/d\eta$, measured in μb per pseudorapidity unit, at the $\sqrt{s} = 500$ and 1000 GeV TESLA linear colliders [47]. Given are the distributions for the Weizsäcker-Williams photon spectrum, the beamstrahlung spectrum and a backscattered laser spectrum.

Figure 21: Transverse momentum cross sections $d\sigma/dp_{\perp}$ at the $\sqrt{s} = 500$ GeV TESLA linear collider [47]. Given are the distributions for the Weizsäcker-Williams photon spectrum, the beamstrahlung spectrum and a backscattered laser spectrum. Please note that the p_{\perp} distributions for the Weizsäcker-Williams spectrum and the beamstrahlung spectrum cross. At low p_{\perp} the beamstrahlung dominates, at high p_{\perp} the W.-W. spectrum dominates.

Figure 22: Decomposition of the jet cross section $d\sigma_{\text{jet}}/dE_{\perp\text{jet}}$ as function of the jet transverse energy. The jets with $E_{\perp\text{jet}} \geq 5$ GeV were found from the PHOJET events using a cone algorithm. The jet acceptance region was restricted to $|\eta_{\text{jet}}| \leq 1.1$.

Figure 23: Jet cross section $d\sigma_{\text{jet}}/dE_{\perp\text{jet}}$ as function of the jet transverse energy. In order to study the influence of multiple soft and hard interactions in the model, we consider restricted cases with only single soft or single hard collisions. The curve with multiple soft, single hard collision coincides nearly with the full curve. The jets with $E_{\perp\text{jet}} \geq 5$ GeV were found from the PHOJET events using a cone algorithm. The jet acceptance region was restricted to $|\eta_{\text{jet}}| \leq 1.1$.

Figure 24: Jet cross section $d\sigma_{\text{jet}}/dE_{\perp\text{jet}}$ as function of the transverse energy. Here we give in addition the cross section with a visible energy cut (inside a calorimeter with $|\eta| \leq 2.1$ the cut is $E_{\text{visible}} \leq 50$ GeV). The jets with $E_{\perp\text{jet}} \geq 5$ GeV were found from the PHOJET events using a cone algorithm. The jet acceptance region was restricted to $|\eta_{\text{jet}}| \leq 1.1$.

Figure 25: Jet profiles in the pseudorapidity variable with and without the visible energy cut described in the caption of Fig. 24.

Figure 26: Cross section as function of the visible energy inside a calorimeter with $|\eta| \leq 2.1$. Only events with $\sqrt{s}_{\gamma\gamma} \geq 10$ GeV are sampled from the improved Weizsäcker-Williams spectrum. In a second curve we request jets with $E_{\perp\text{jet}} \geq 5$ GeV and impose a visible energy cut of 50 GeV.

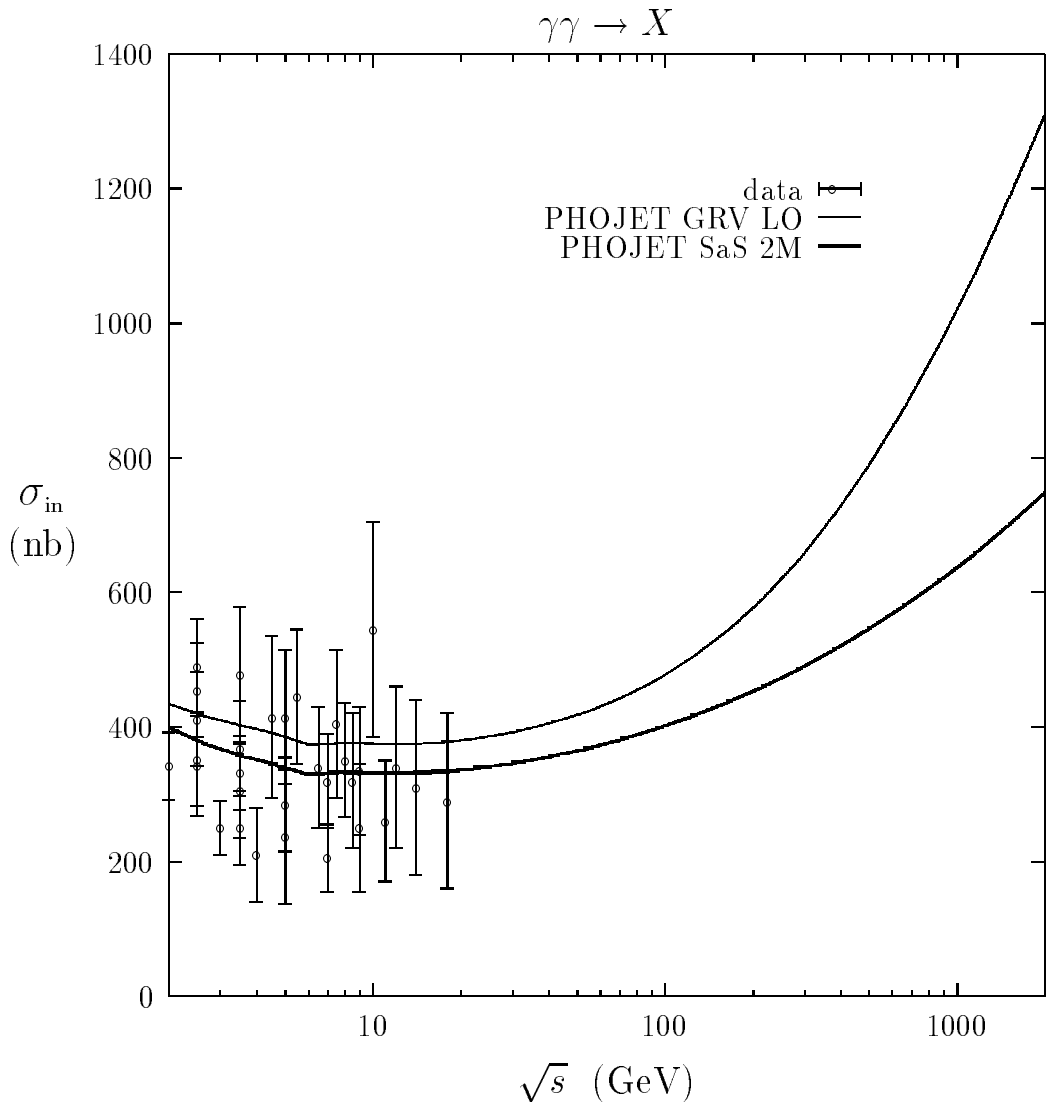


Figure 1: Inelastic photon-photon cross sections as calculated in the model compared with experimental data at low energies [48, 49, 50, 51, 52]. The two curves from the model were calculated using the GRV LO photon structure function [17] and the SaS 2M photon structure function [53]. The differences between both curves at high energy demonstrate the uncertainties of the predictions due to the limited data available on the photon structure function. Our curve calculated with the SaS 2M structure function agrees practically with the cross section calculated with the same structure function but using another model by Schuler and Sjöstrand [54].

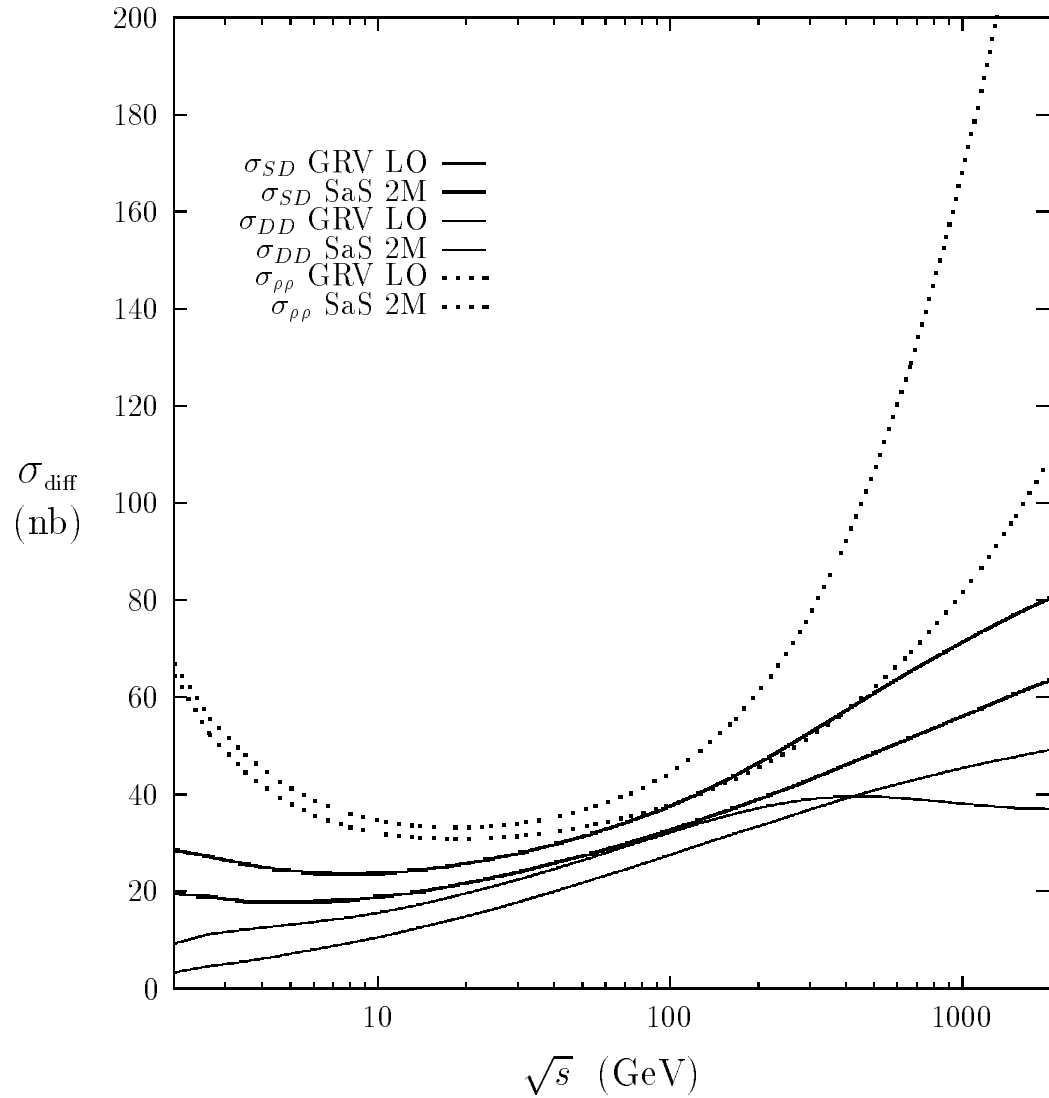


Figure 2: Diffractive cross sections as calculated with PHOJET using the GRV LO photon structure function [17] and the SaS 2M photon structure function [53]. The upper curve is for each of the three cross sections the one obtained with the GRV LO structure function.

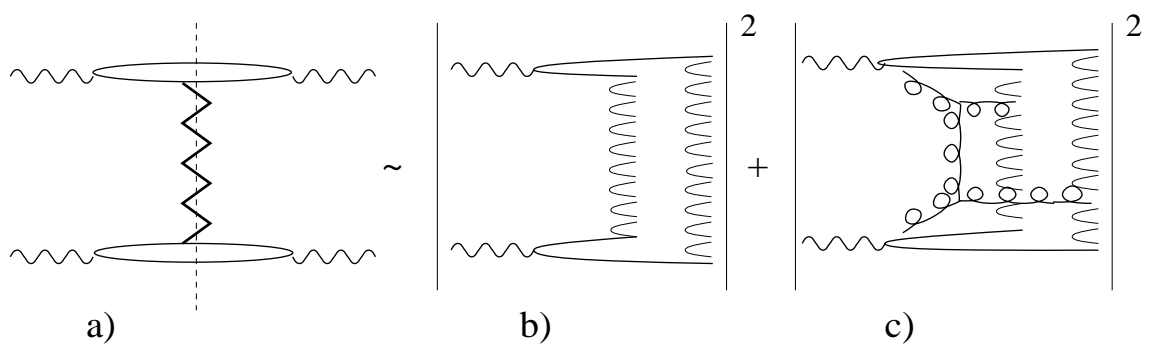


Figure 3: Unitarity cut of a one-pomeron graph: the unitarity sum including all possible final states is subdivided into final states with low- p_\perp partons and into final states with at least one parton satisfying $p_\perp \geq p_\perp^{\text{cutoff}}$.

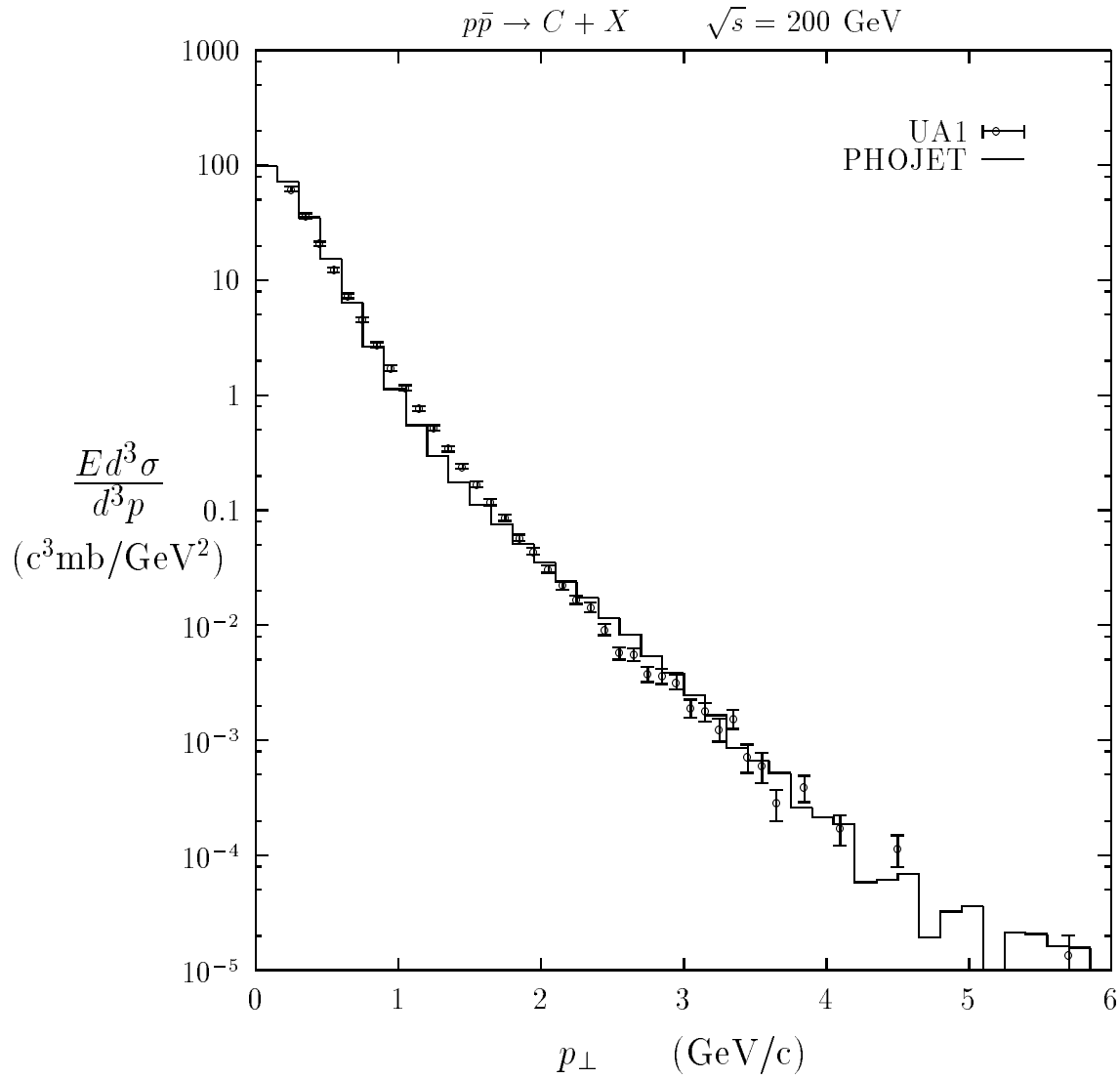


Figure 4: Comparison of transverse momentum distributions of charged hadrons with collider data at $\sqrt{s} = 200$ GeV [32]. The calculation uses the Dual Parton Model code PHOJET.

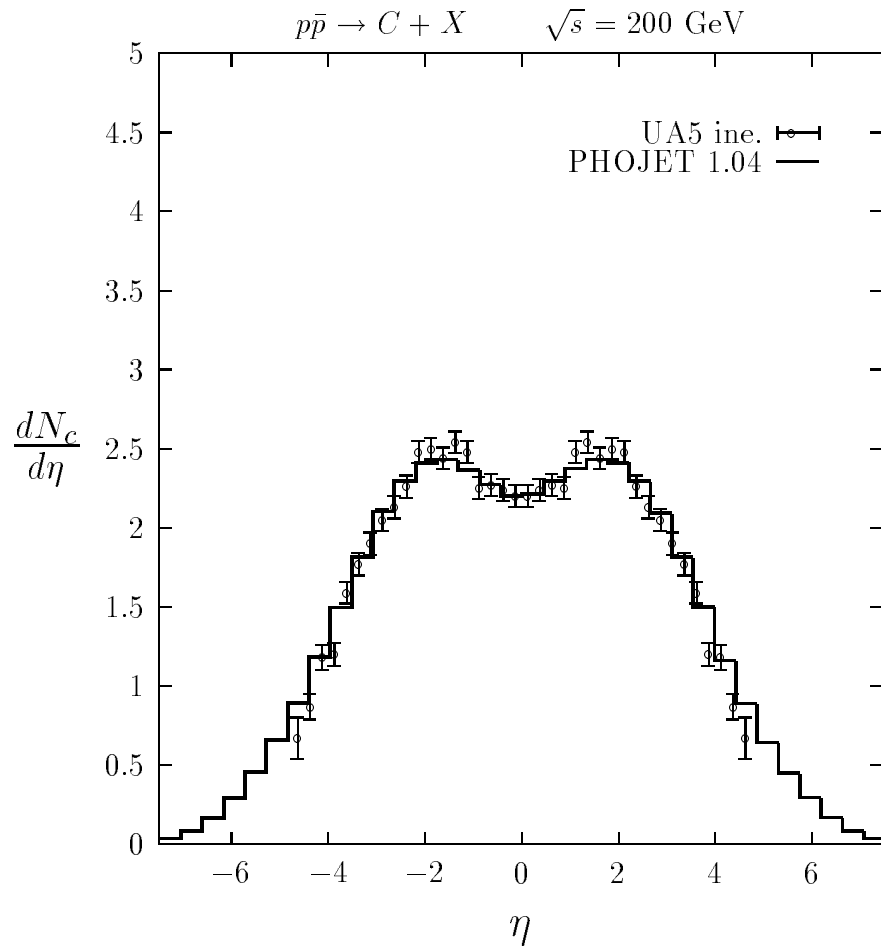


Figure 5: Pseudorapidity distributions of charged hadrons produced in \bar{p} - p collisions as calculated with PHOJET are compared to collider data from the UA-5 Collaboration [33, 34] for the energy $\sqrt{s} = 200$ GeV.

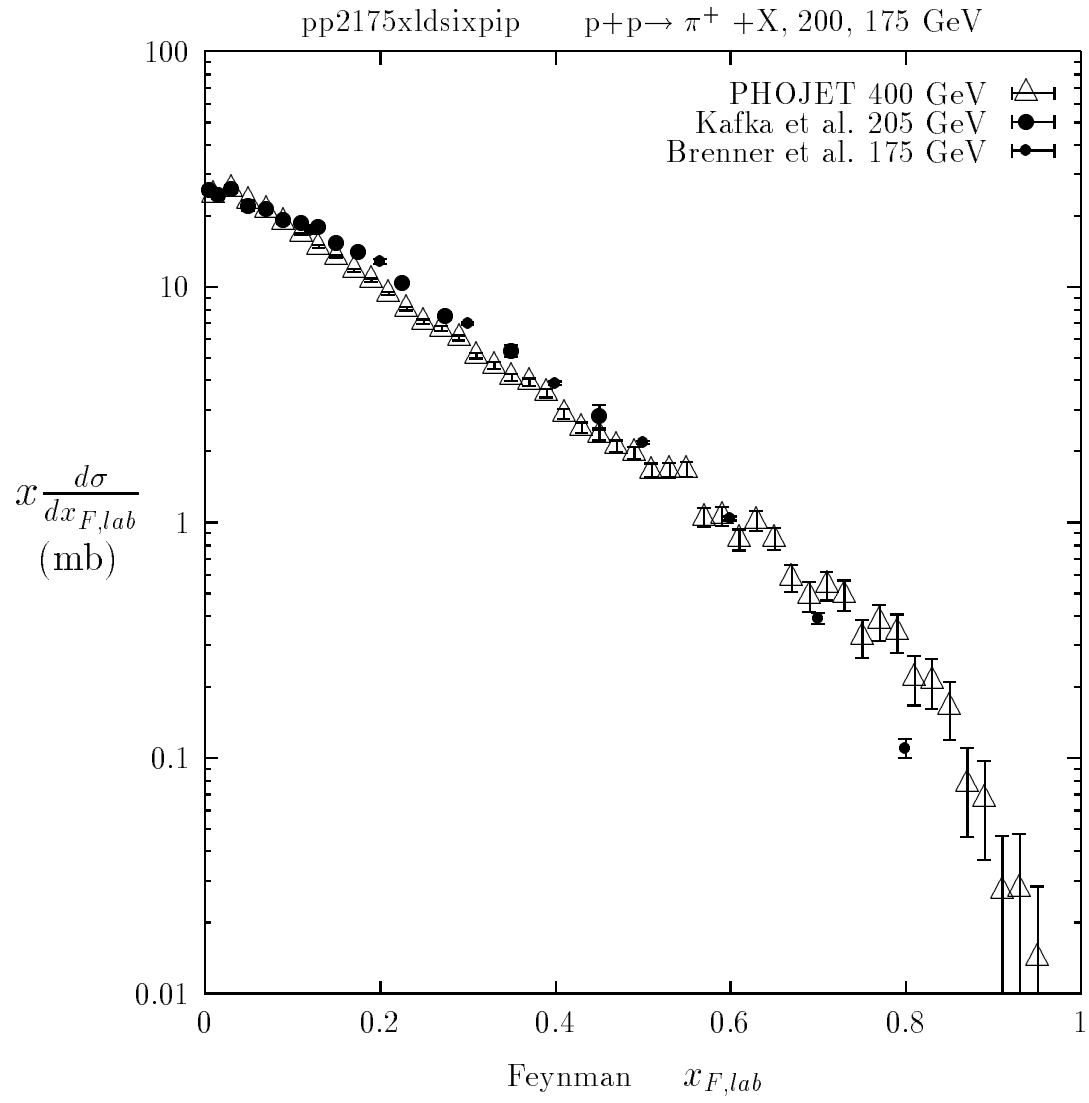


Figure 6: Comparison of Feynman x_F distributions of π^+ -mesons produced in proton-proton collisions at 205 and 175 GeV. The experimental data are from Kafka et al. [55] and from Brenner et al. [56]. The data from both experiments agree rather well with each other. The calculation uses the Dual Parton Model PHOJET.

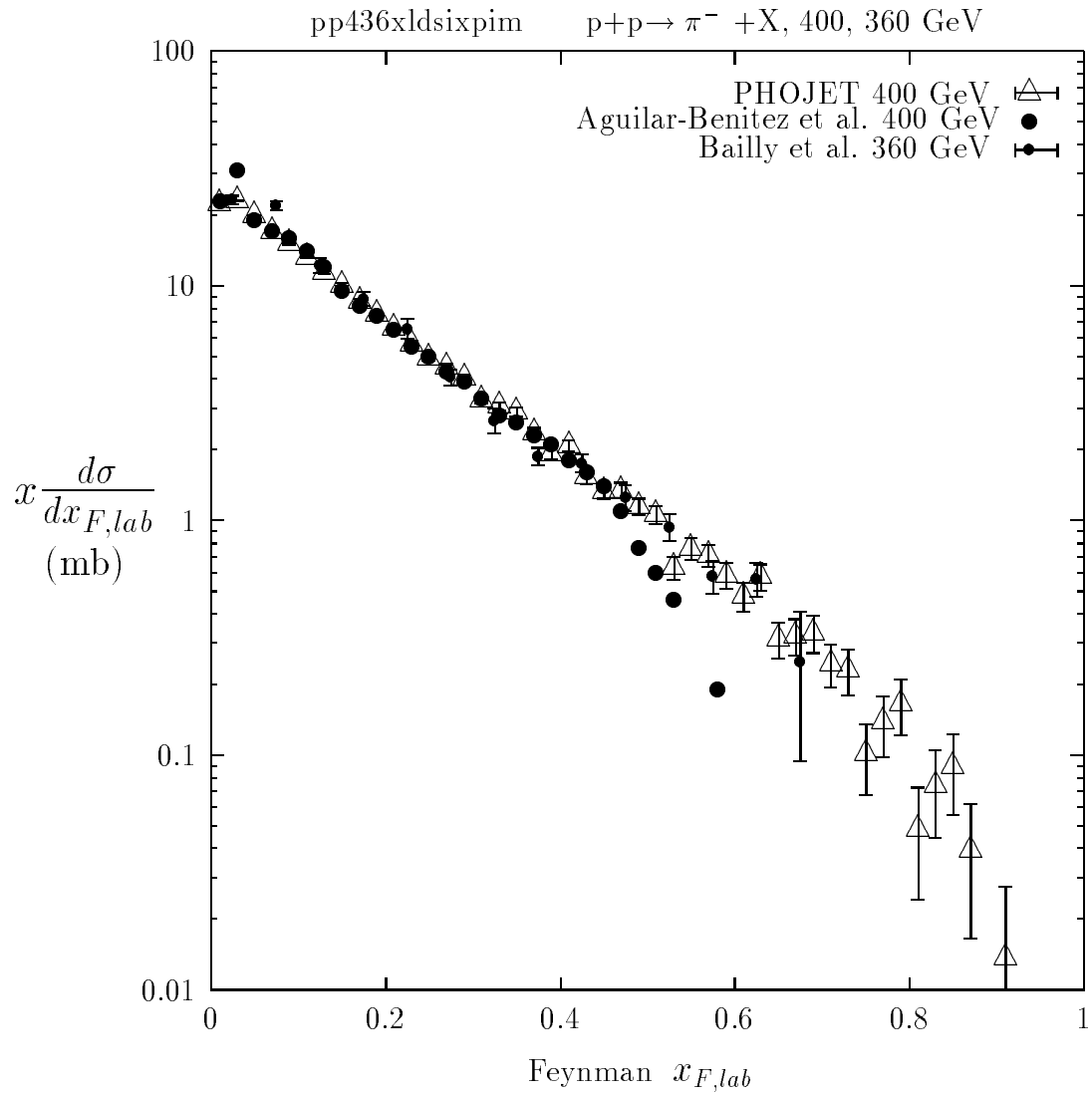


Figure 7: Comparison of Feynman x_F distributions of π^- -mesons produced in proton-proton collisions at 400 and 360 GeV. The experimental data are from the Aguilar-Benitez et al. [57] and from the EHS-RCBC Collaboration [58]. The data from both experiments agree rather well with each other, in fact most of the data points of [58] are below the [57] data. The calculation uses the Dual Parton Model PHOJET.

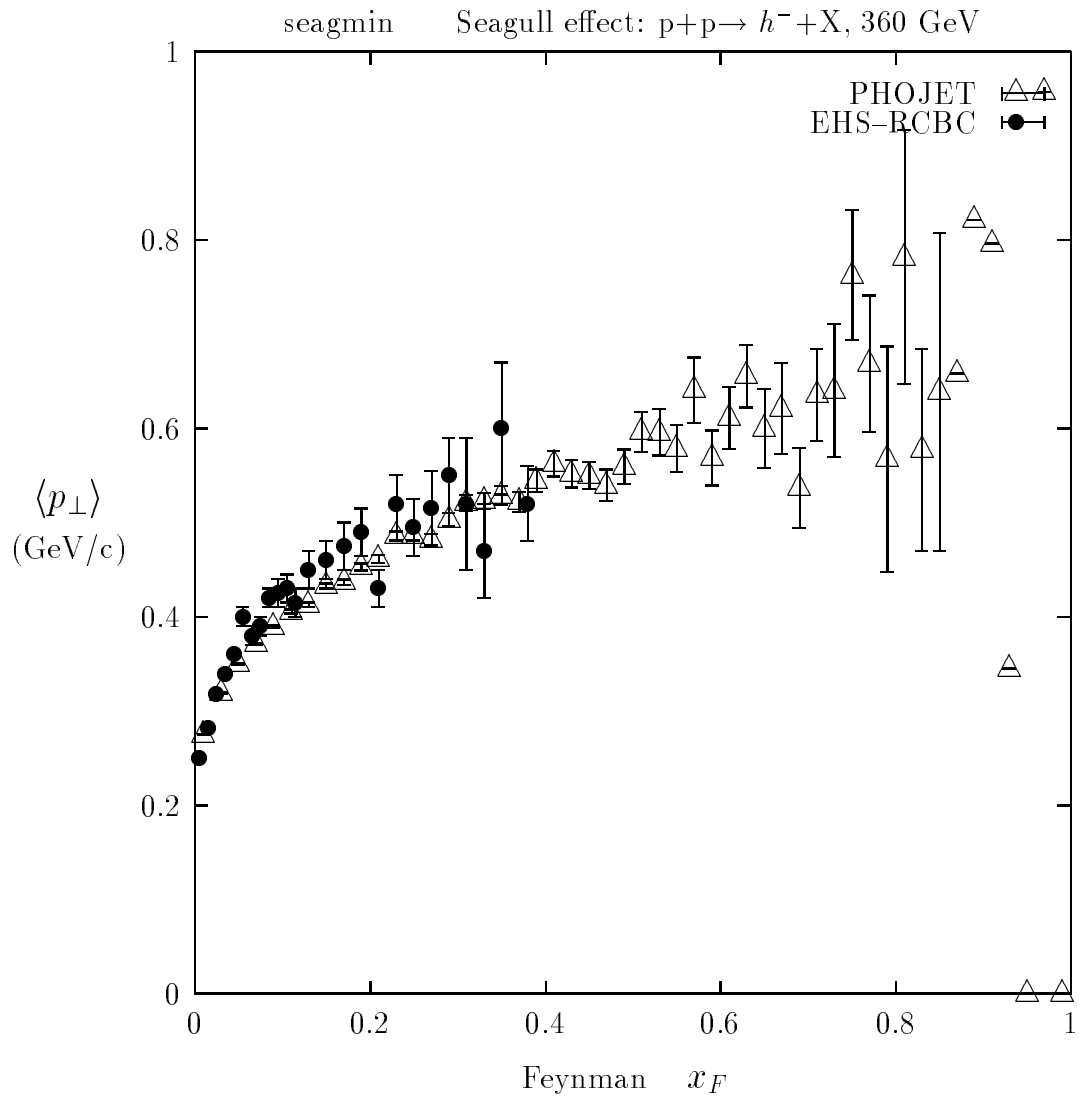


Figure 8: Comparison of the seagull effect in the reaction $p+p \rightarrow h^- + X$ at 360 GeV. The data are from the EHS-RCBC Collaboration [35]. The calculation uses the Dual Parton Model PHOJET.

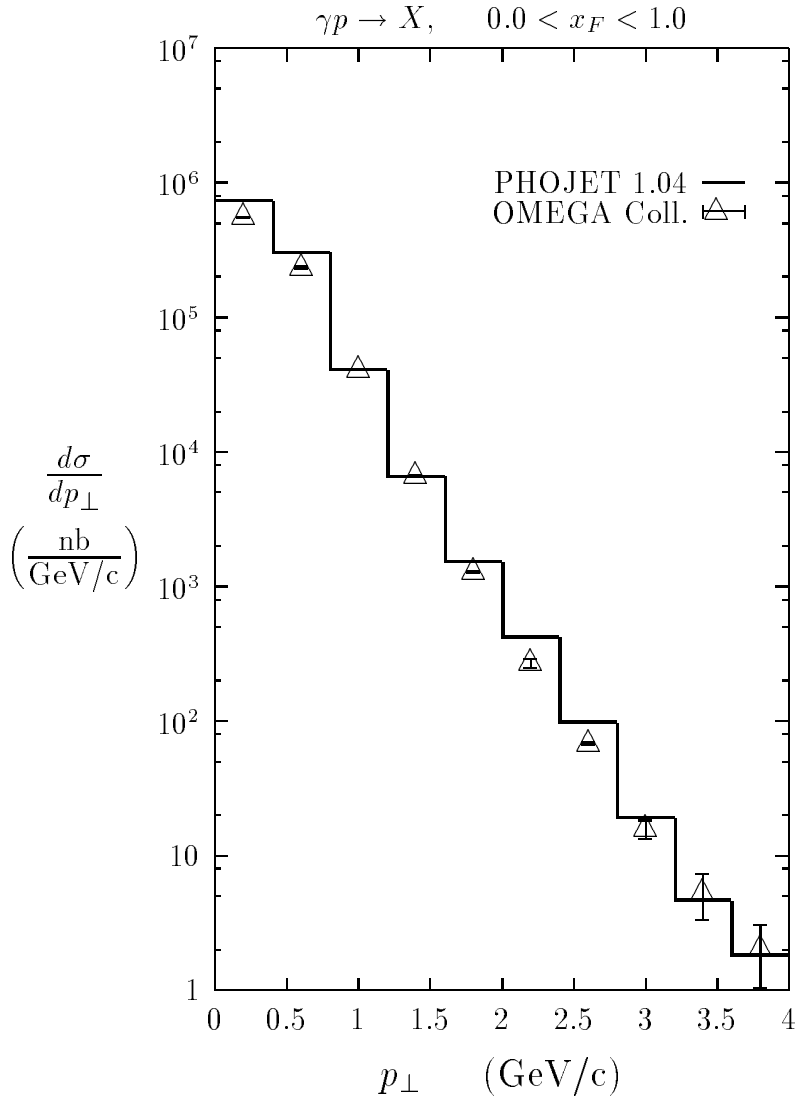


Figure 9: Comparison of the transverse momentum distribution of charged hadrons with $0 \leq x_F \leq 1$ as calculated with PHOJET at the average photon energy of 140 GeV with data. The data are from the OMEGA Collaboration [36] measured with a tagged photon beam in the energy band 110-170 GeV.

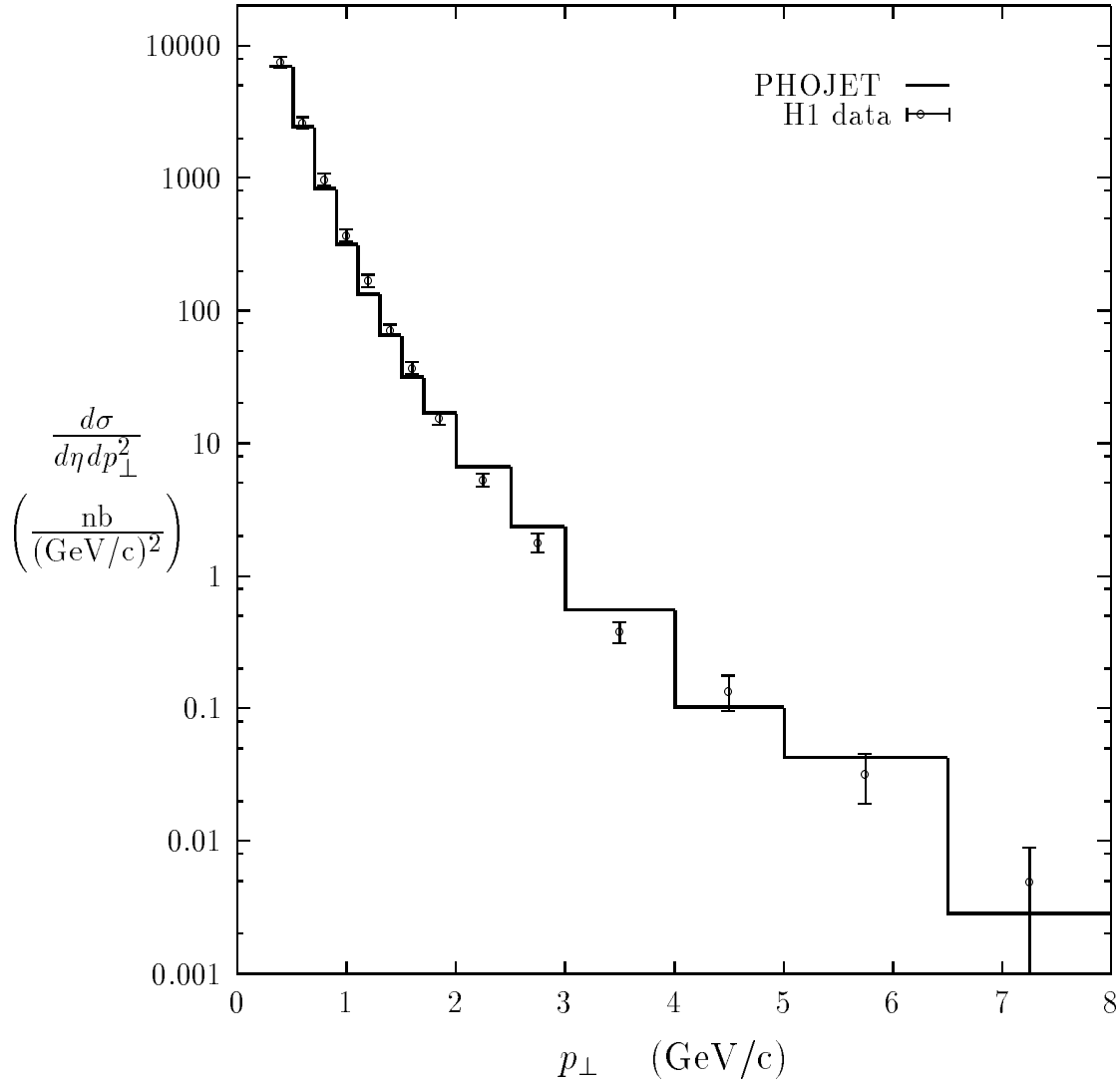


Figure 10: Comparison of the transverse momentum distribution of charged hadrons produced by quasi-real photons in electron-proton collisions at HERA [37] with the PHOJET calculation [10]. The data and the calculation is in the pseudorapidity region $-1.5 \leq \eta_{\text{lab}} \leq 1.5$.

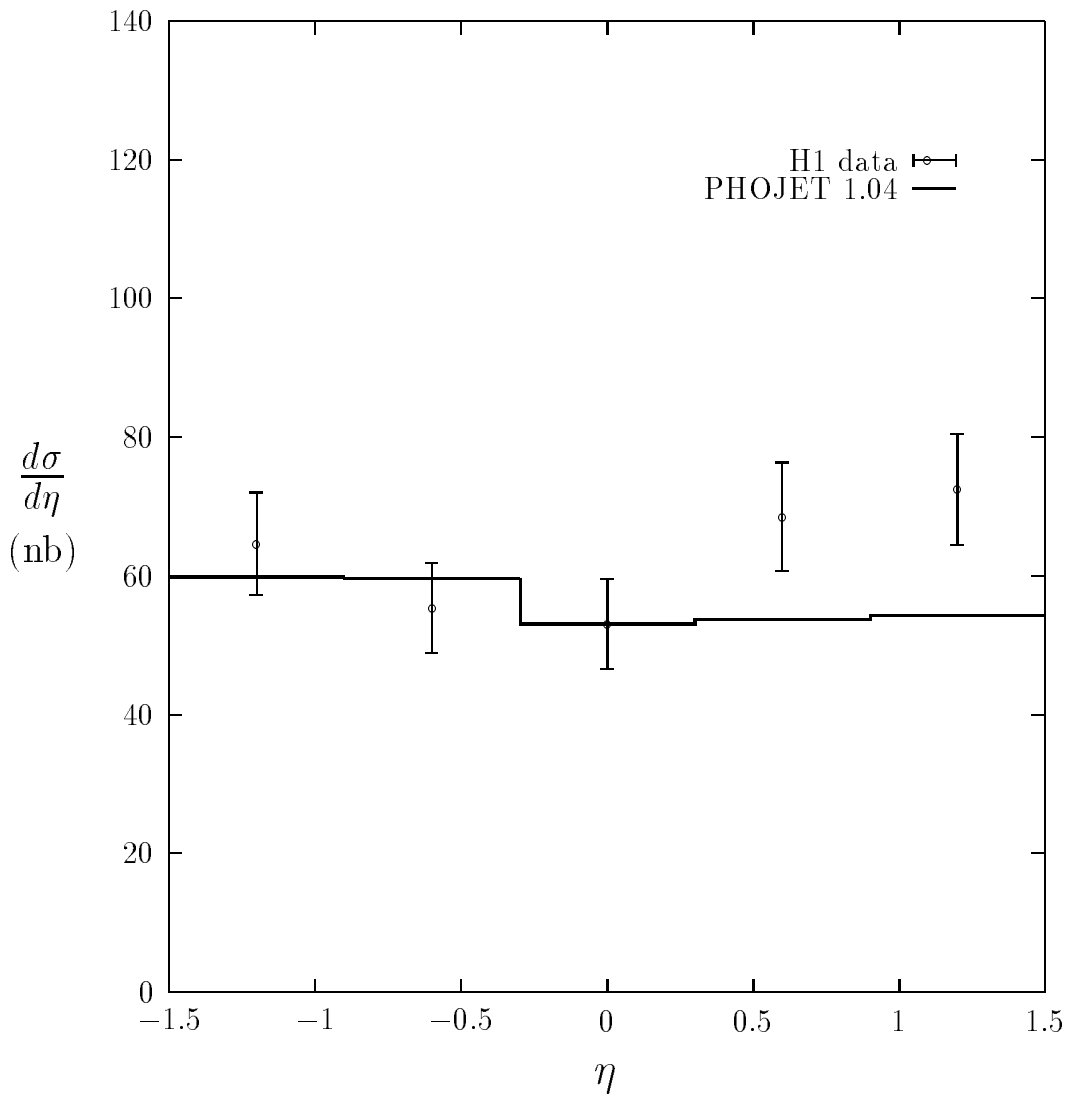


Figure 11: Comparison of the inclusive pseudorapidity cross section of charged hadrons produced by quasi-real photons in electron-proton collisions at HERA [37] with the PHOJET calculation [10].

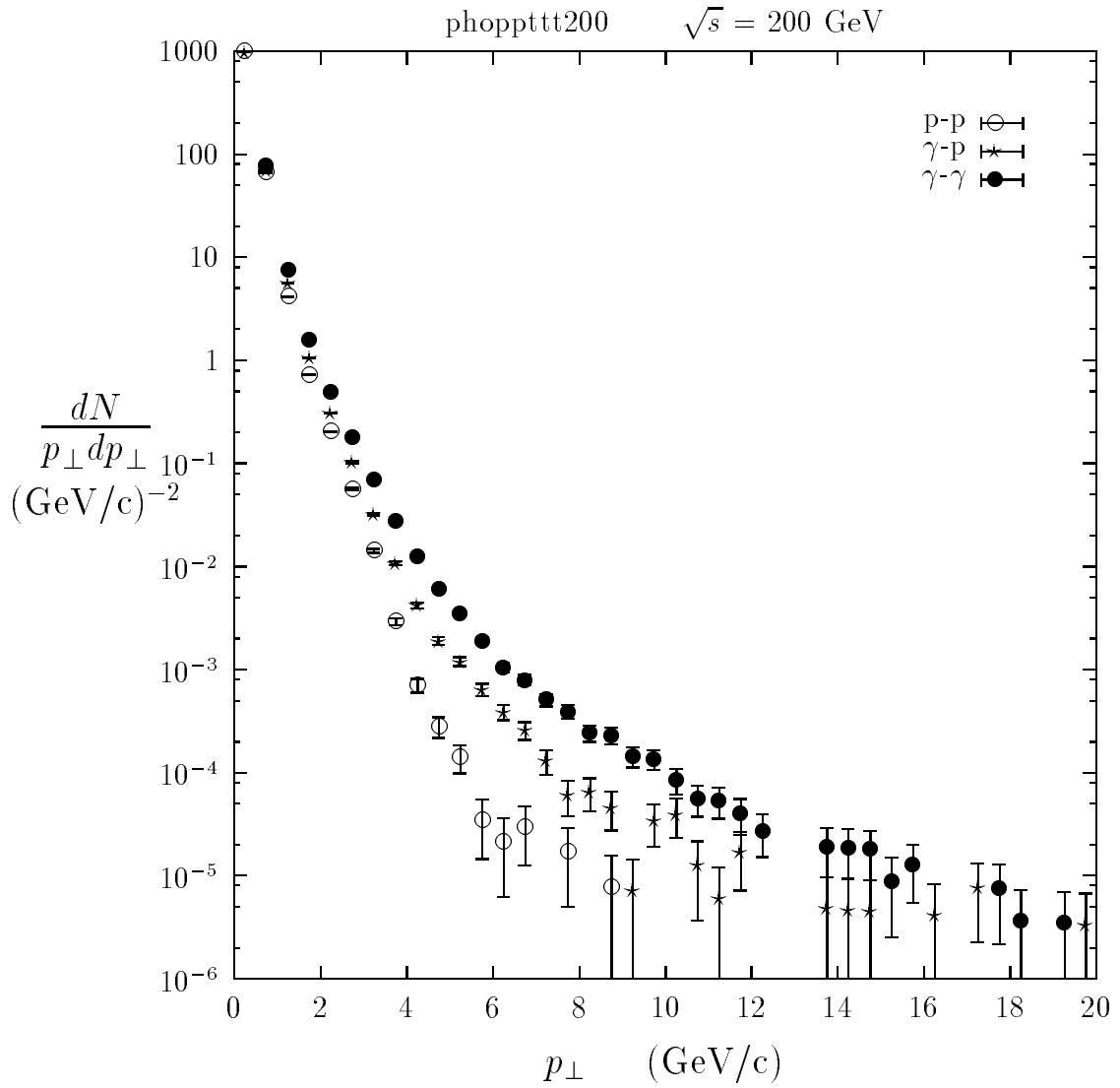


Figure 12: We compare at the collision energy $\sqrt{s} = 200$ GeV the transverse momentum distribution in invariant form for all charged hadrons produced in proton-proton, photon-proton and photon-photon collisions. The calculation was done with PHOJET for inelastic collisions, excluding in photon-proton collisions the V - p and in photon-photon collisions the V - V diffractive production of vector mesons $V = \rho, \omega$ and ϕ .

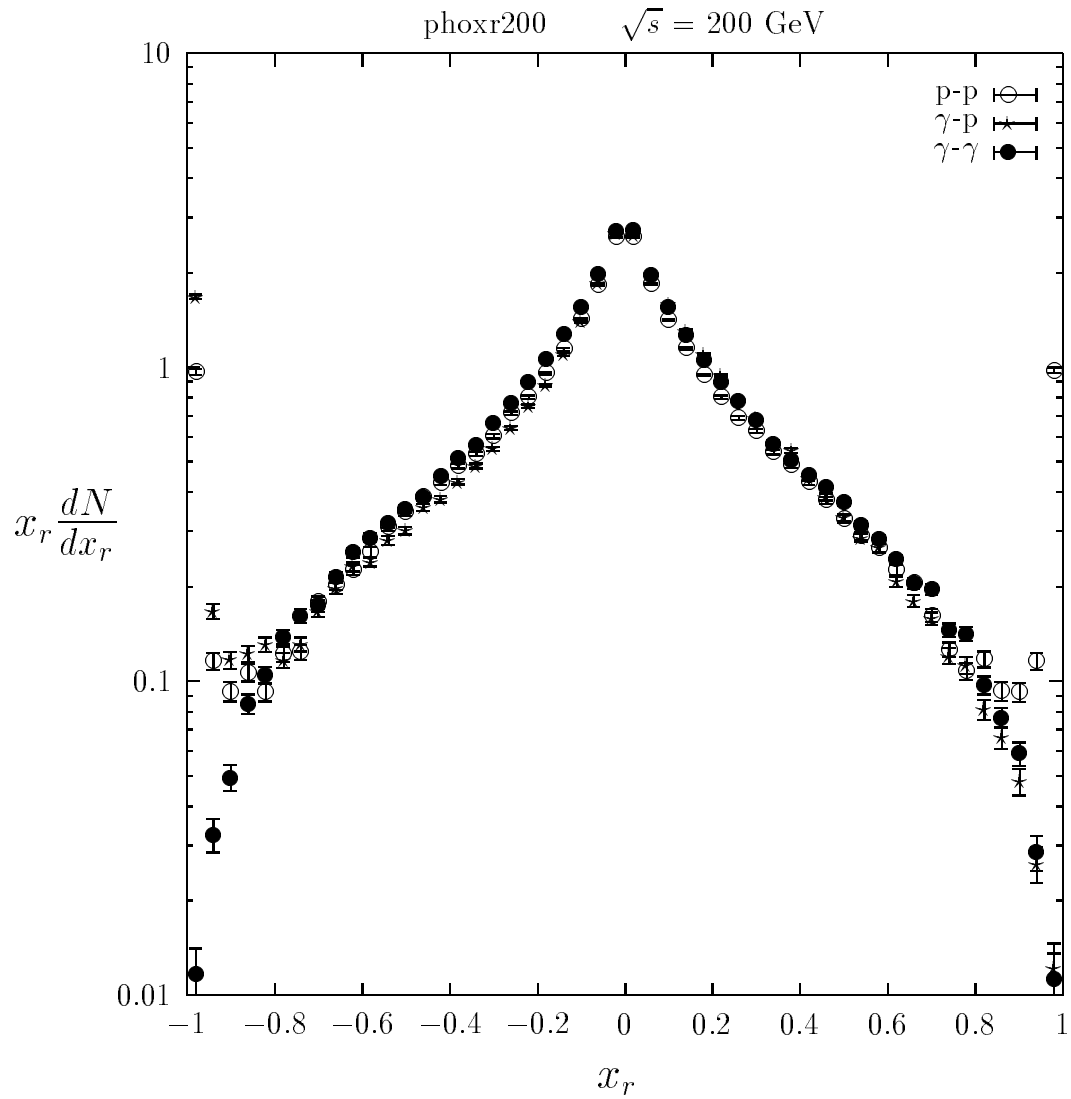


Figure 13: We compare at the collision energy $\sqrt{s} = 200$ GeV the radial $x_r = 2E/\sqrt{s}$ distribution in invariant form for all charged hadrons produced in proton-proton, photon-proton and photon-photon collisions. The calculation was done with PHOJET for inelastic collisions, excluding in photon-proton collisions the $V\text{-}p$ and in photon-photon collisions the $V\text{-}V$ diffractive contributions.

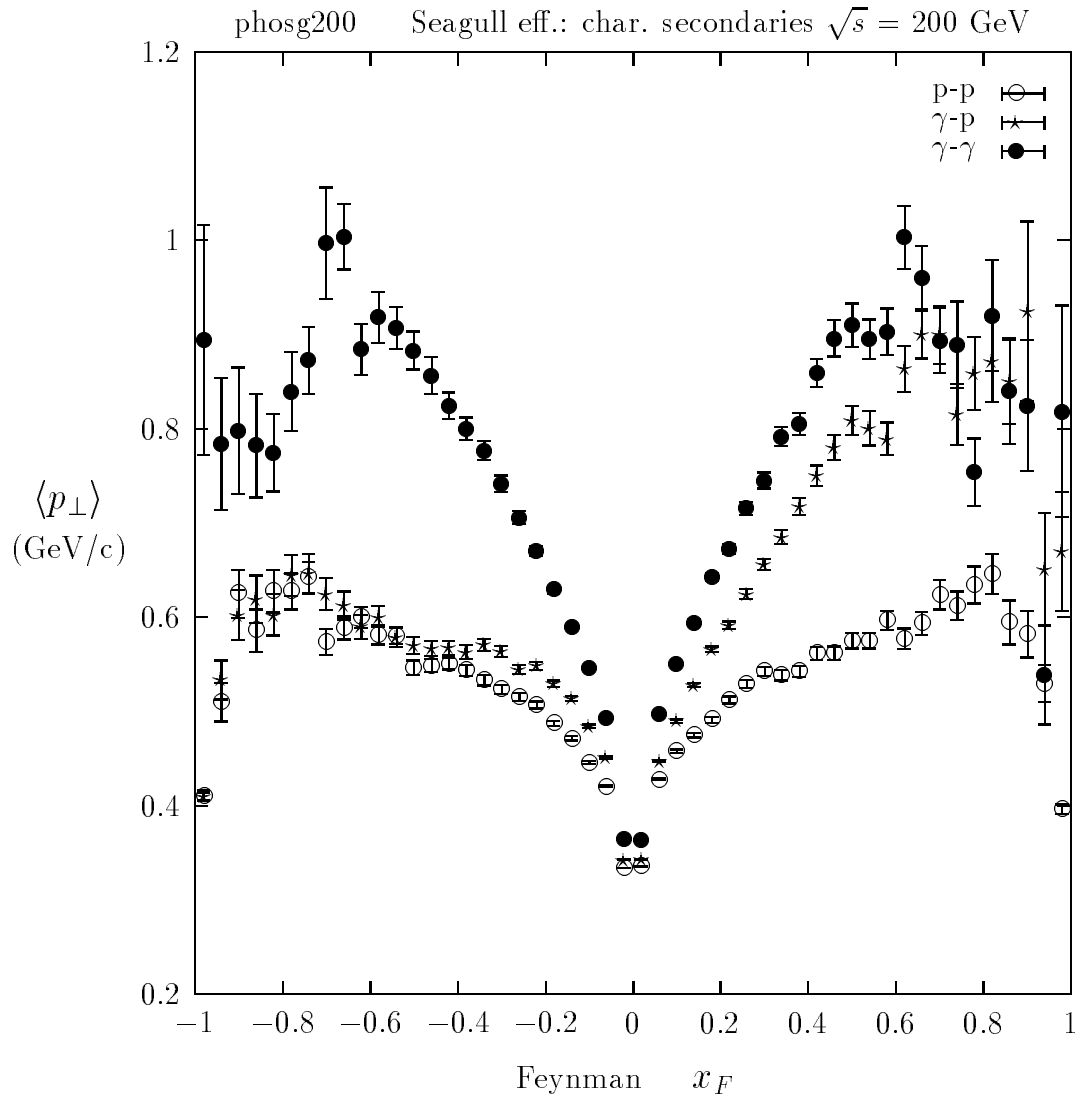


Figure 14: We compare at the collision energy $\sqrt{s} = 200$ GeV the average transverse momentum of charged hadrons produced in proton-proton, photon-proton and photon-photon collisions as function of the Feynman x_F variable (seagull effect). The calculation was done with PHOJET for inelastic collisions, excluding in photon-proton collisions the V - p and in photon-photon collisions the V - V diffractive contributions.

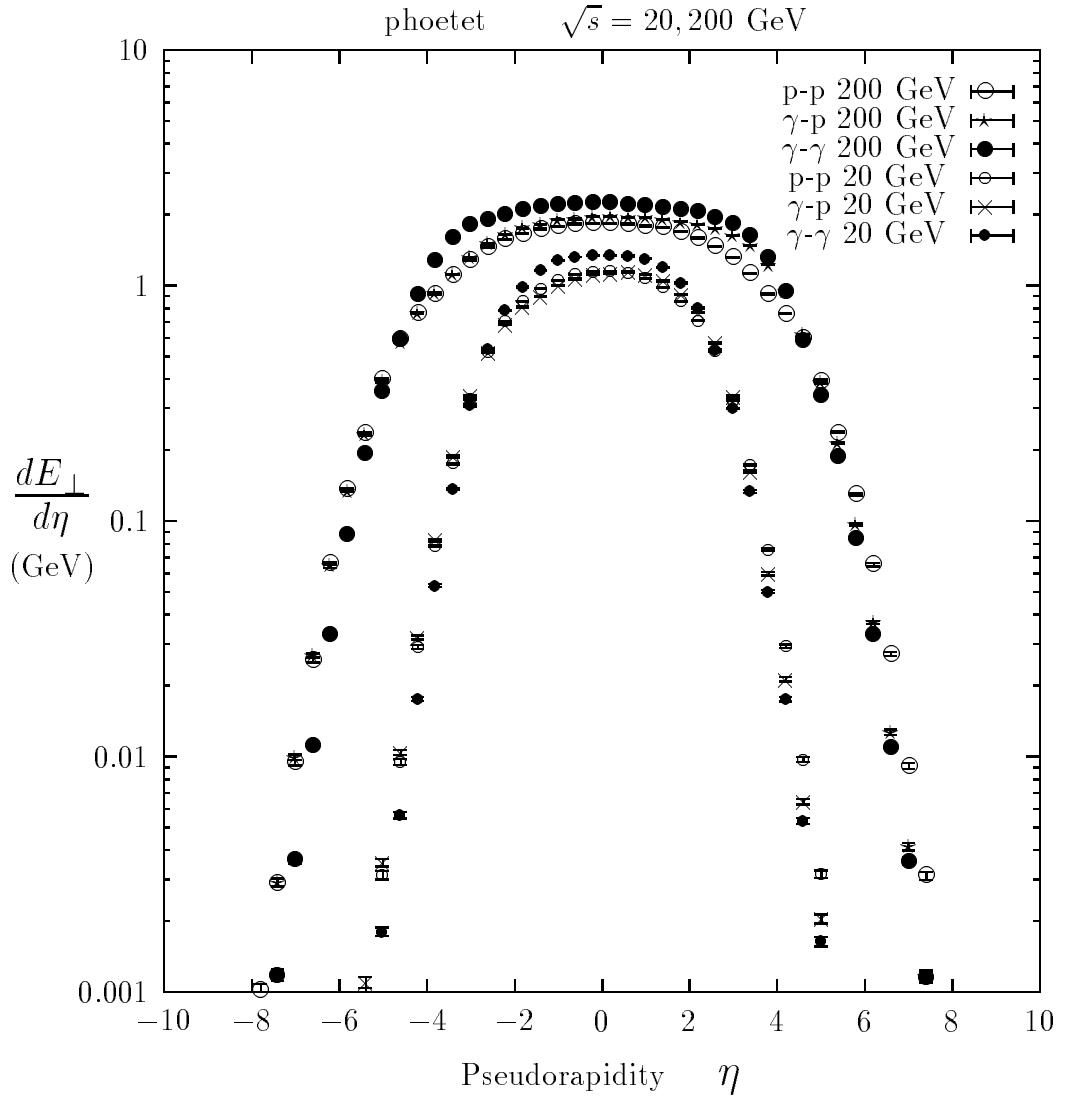


Figure 15: We compare at the collision energies $\sqrt{s} = 20$ GeV and 200 GeV in a log-plot the distribution of the transverse energy E_{\perp} as function of the pseudorapidity η for proton-proton, photon-proton and photon-photon collisions. The calculation was done with PHOJET for inelastic collisions, excluding in photon-proton collisions the V - p and in photon-photon collisions the V - V diffractive contributions.

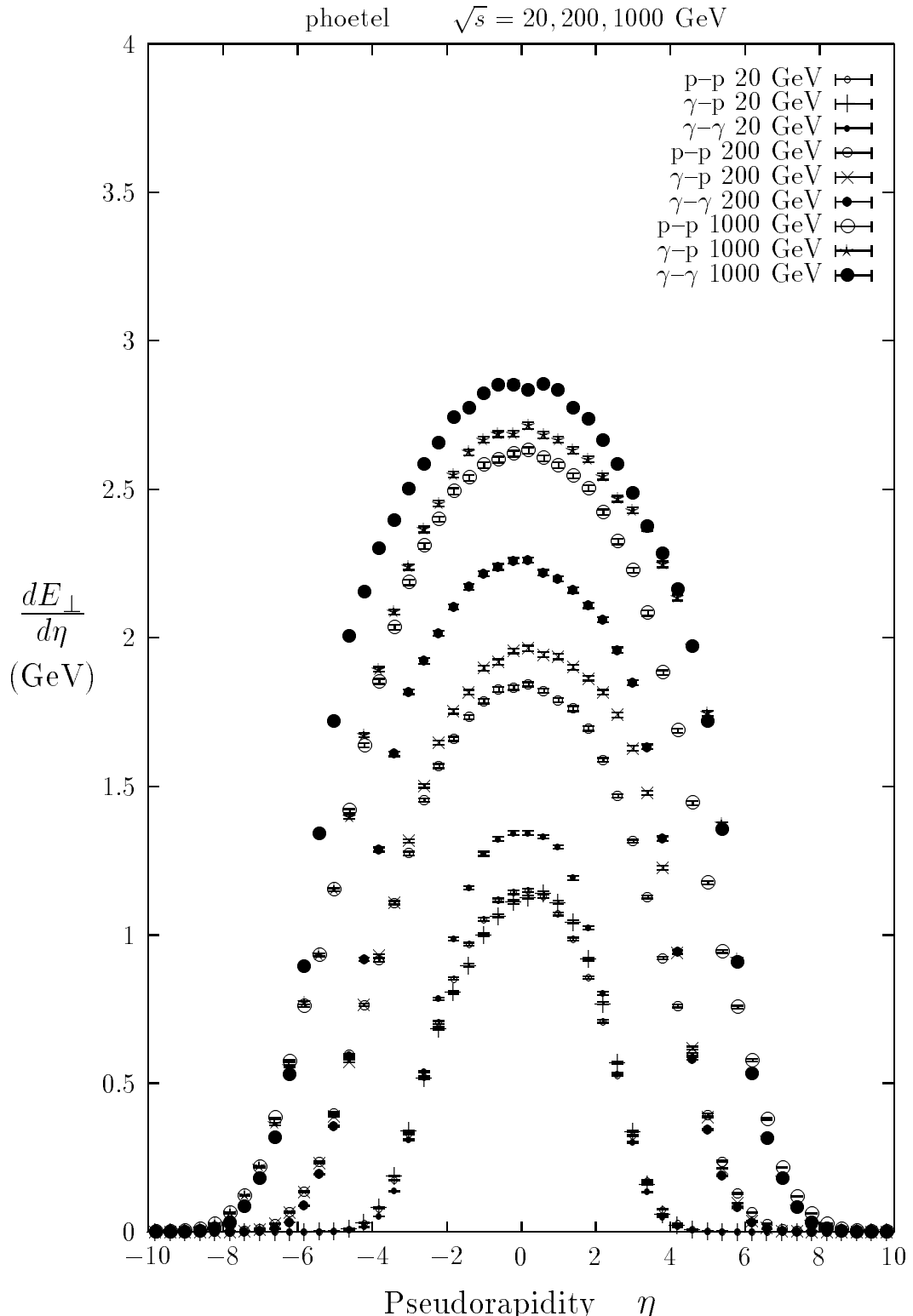


Figure 16: We compare at the collision energies $\sqrt{s} = 20$ GeV, 200 GeV and 1000 GeV in a linear plot the distribution of the transverse energy E_{\perp} as function of the pseudorapidity η for proton-proton, photon-proton and photon-photon collisions. The calculation was done with PHOJET for inelastic collisions, excluding in photon-proton collisions the V - p and in photon-photon collisions the V - V diffractive contributions.

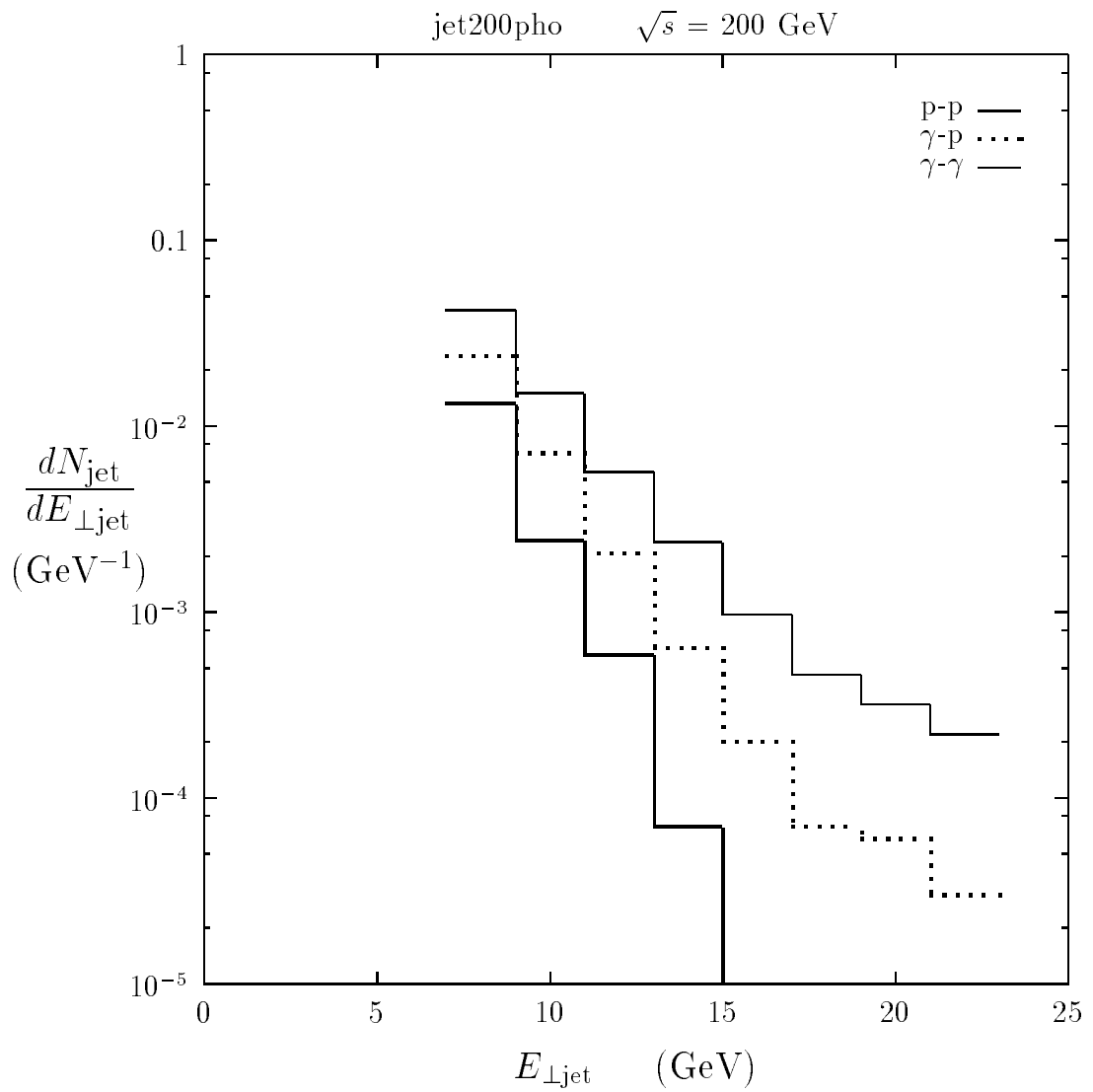


Figure 17: We compare at the collision energy $\sqrt{s} = 200$ GeV the transverse energy distribution for hadronic jets (identified using a jet-finding algorithm) produced in proton-proton, photon-proton and photon-photon collisions. The calculation was done with PHOJET.

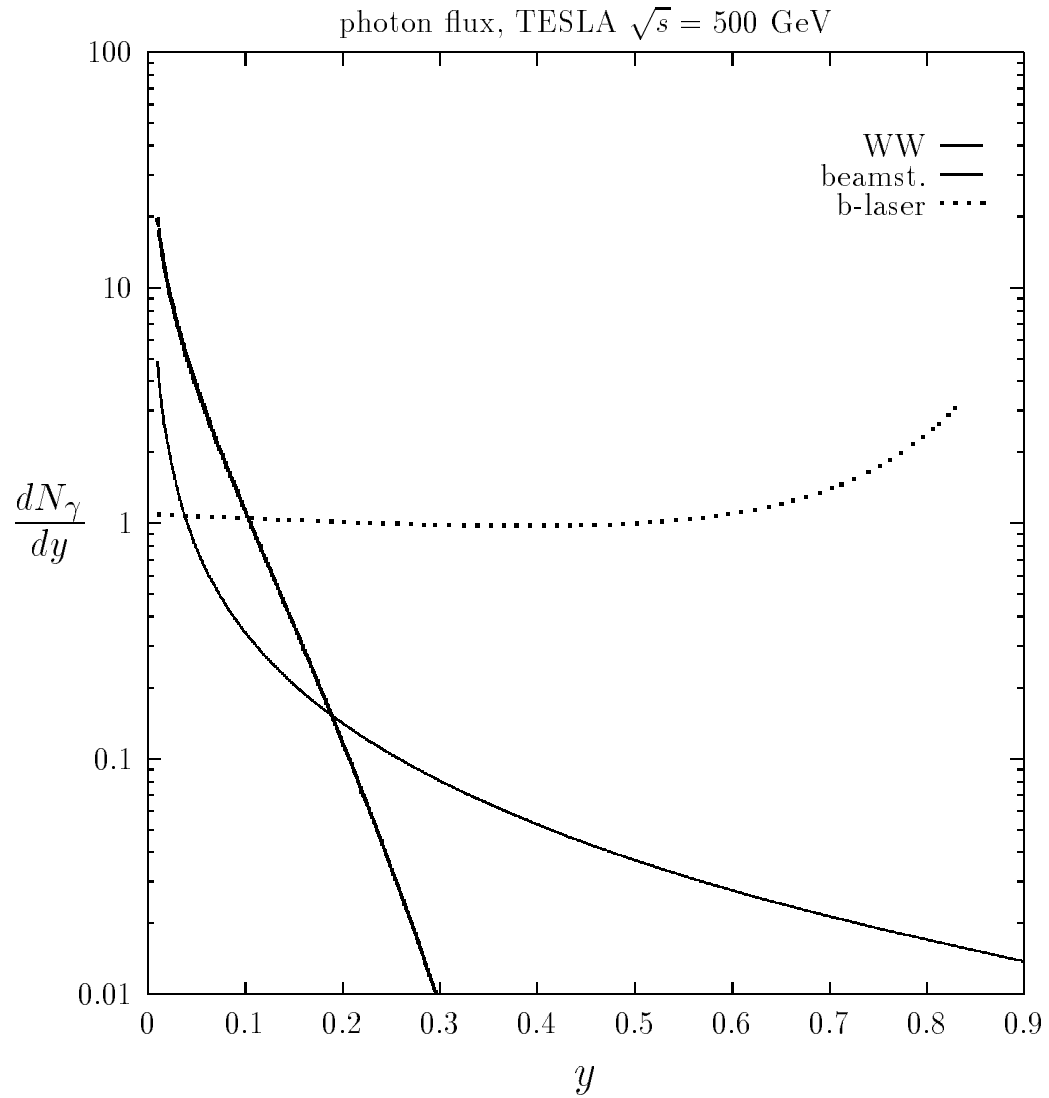


Figure 18: Photon fluxes at a $\sqrt{s} = 500$ GeV linear collider TESLA [47]. Given are the improved Weizsäcker-Williams spectrum, the beamstrahlung spectrum using the bunch parameters $N_e = 1.8 \cdot 10^{10}$, $\sigma_x = 598$ nm, $\sigma_y = 6.5$ nm and $\sigma_z = 0.5$ mm [47], and a backscattered laser spectrum.

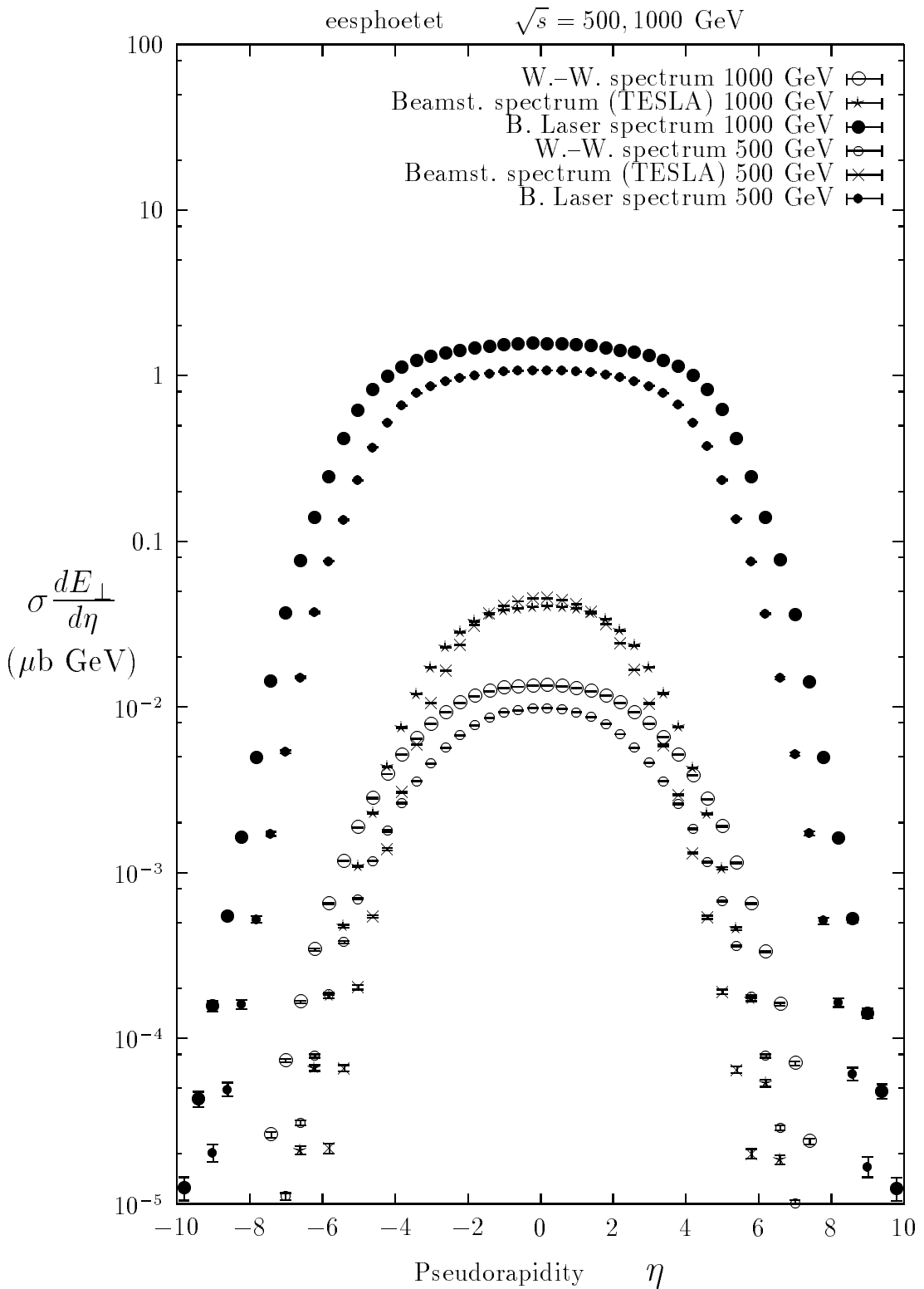


Figure 19: Cross section weighted transverse energy distributions $\sigma dE_{\perp}/d\eta$ measured in $\mu\text{b GeV}$ at the $\sqrt{s} = 500$ and 1000 GeV TESLA linear colliders [47]. Given are the distributions for the Weizsäcker-Williams photon spectrum, the beamstrahlung spectrum and a backscattered laser spectrum.

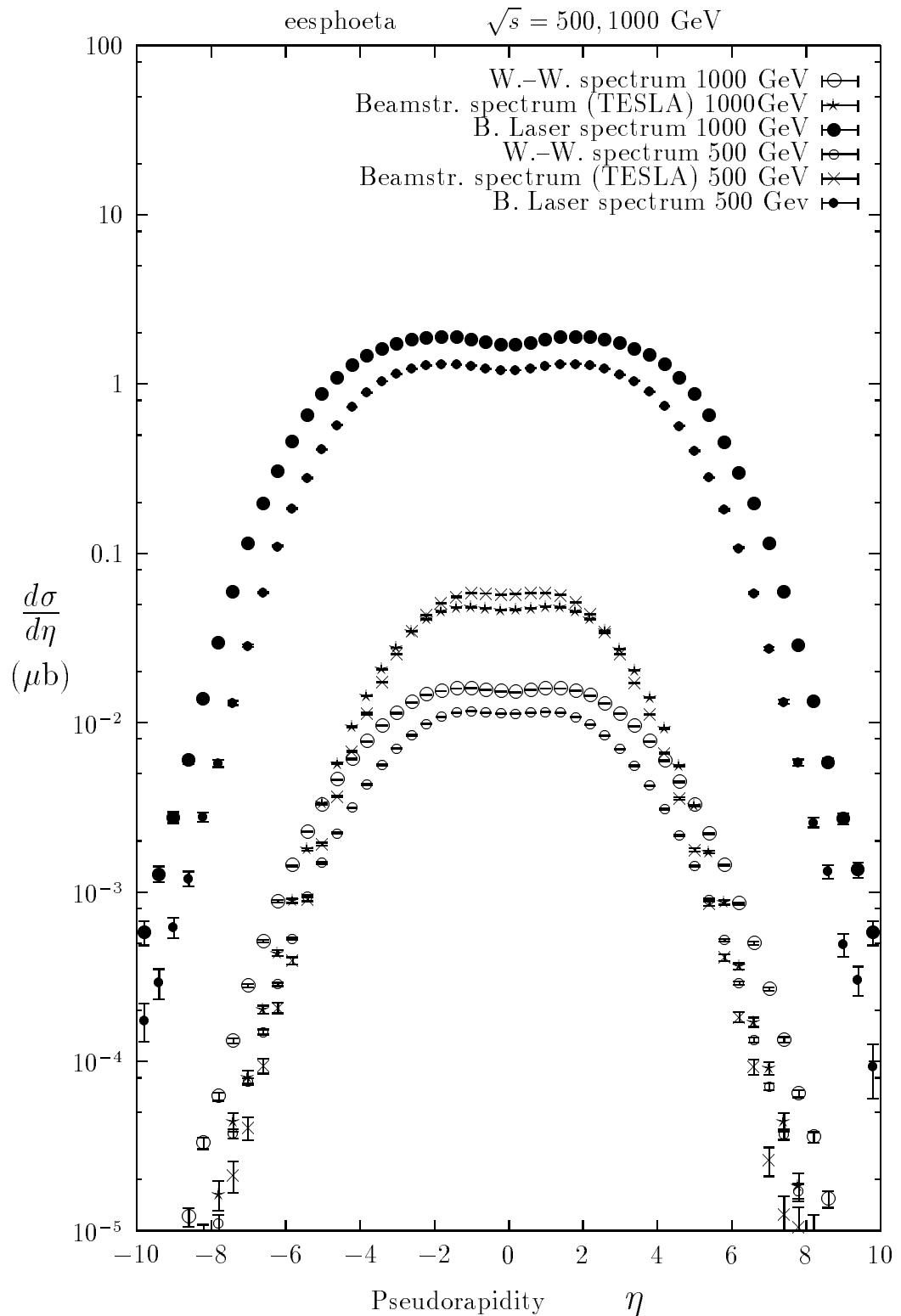


Figure 20: Pseudorapidity cross sections $d\sigma/d\eta$, measured in μb per pseudorapidity unit, at the $\sqrt{s} = 500$ and 1000 GeV TESLA linear colliders [47]. Given are the distributions for the Weizsäcker-Williams photon spectrum, the beamstrahlung spectrum and a backscattered laser spectrum.

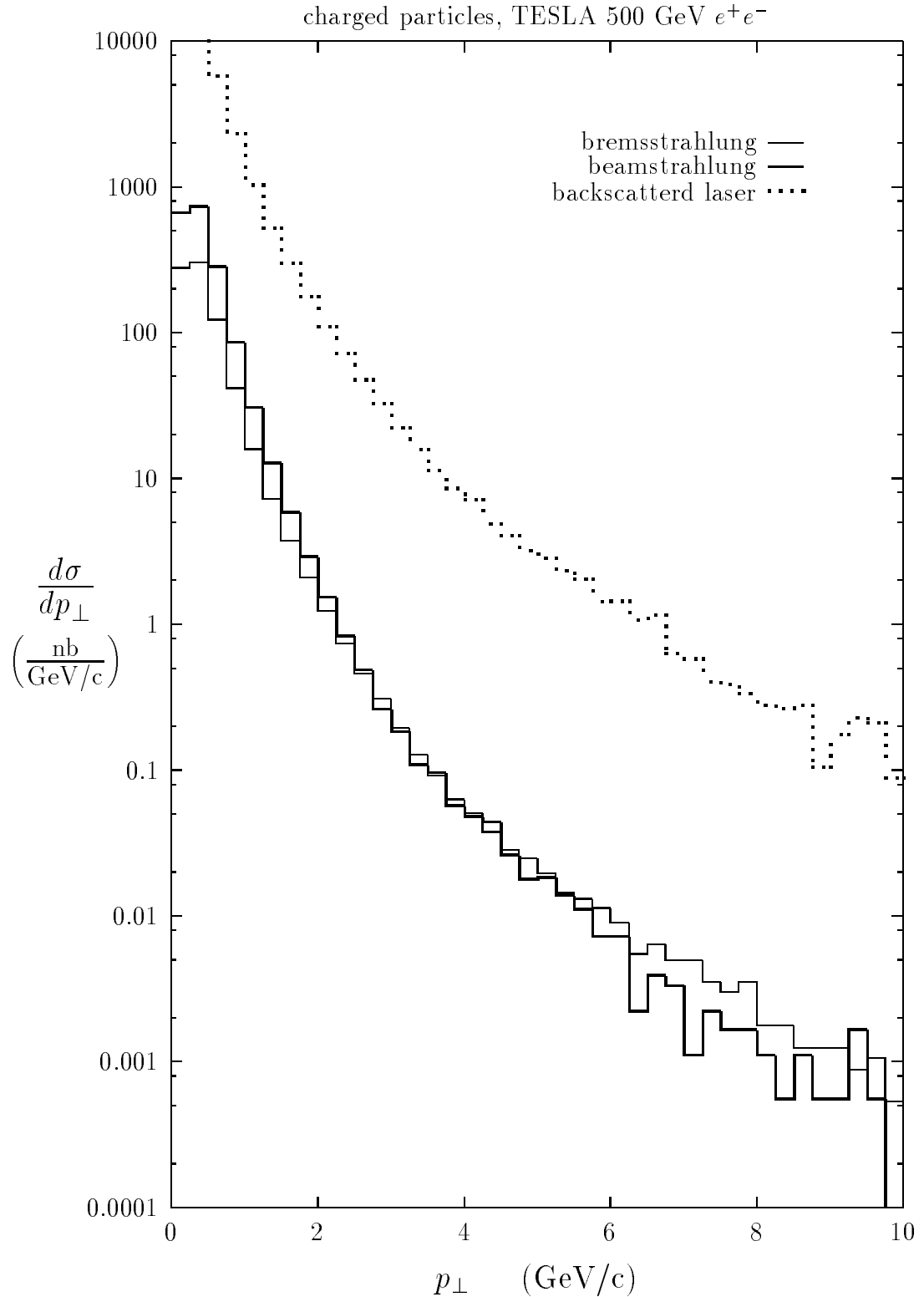


Figure 21: Transverse momentum cross sections $d\sigma/dp_\perp$ at the $\sqrt{s} = 500$ GeV TESLA linear collider [47]. Given are the distributions for the Weizsäcker-Williams photon spectrum, the beamstrahlung spectrum and a backscattered laser spectrum. Please note that the p_\perp distributions for the Weizsäcker-Williams spectrum and the beamstrahlung spectrum cross. At low p_\perp the beamstrahlung dominates, at high p_\perp the W.-W. spectrum dominates.

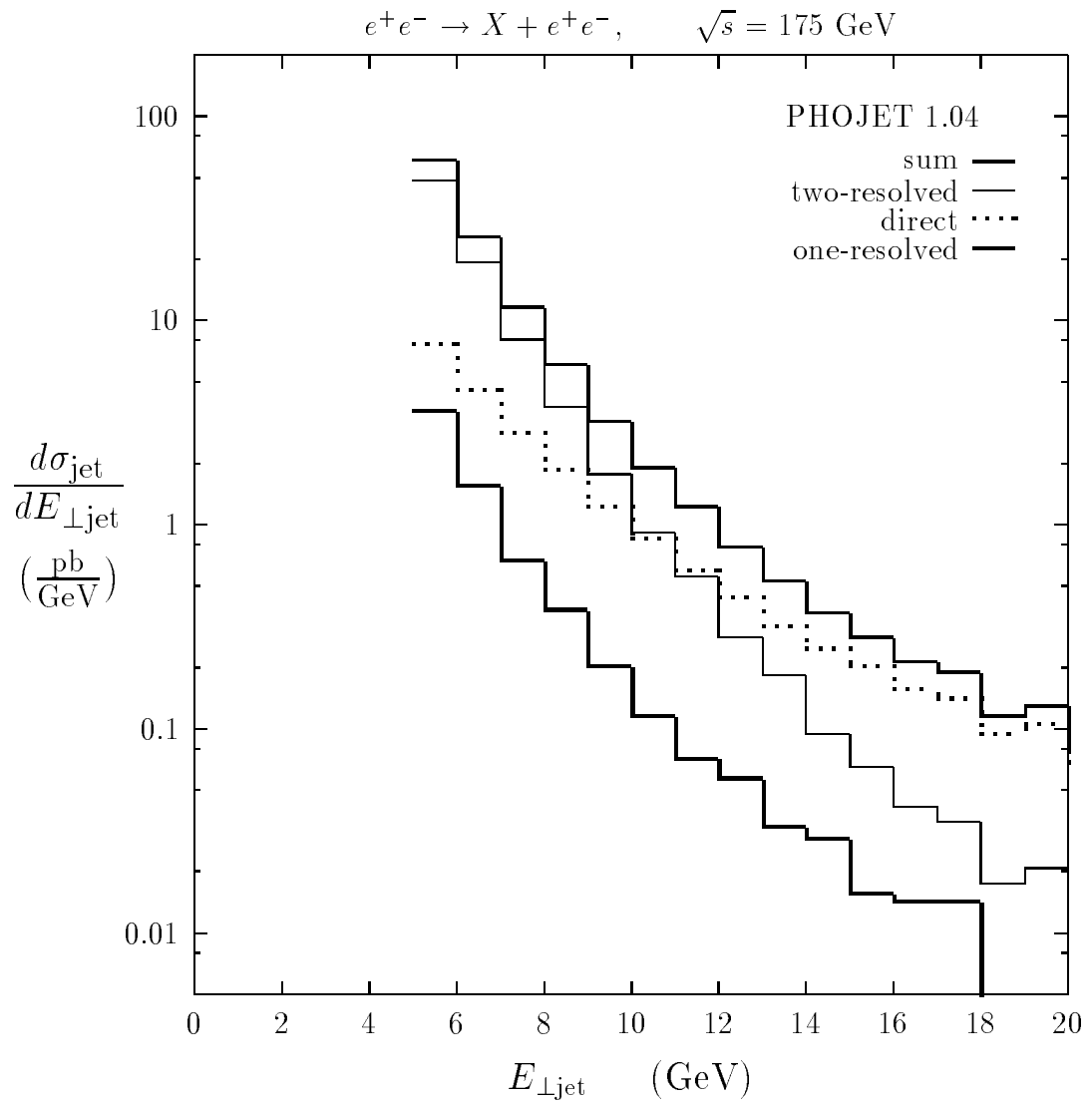


Figure 22: Decomposition of the jet cross section $d\sigma_{\text{jet}}/dE_{\perp\text{jet}}$ as function of the jet transverse energy. The jets with $E_{\perp\text{jet}} \geq 5$ GeV were found from the PHOJET events using a cone algorithm. The jet acceptance region was restricted to $|\eta_{\text{jet}}| \leq 1.1$.

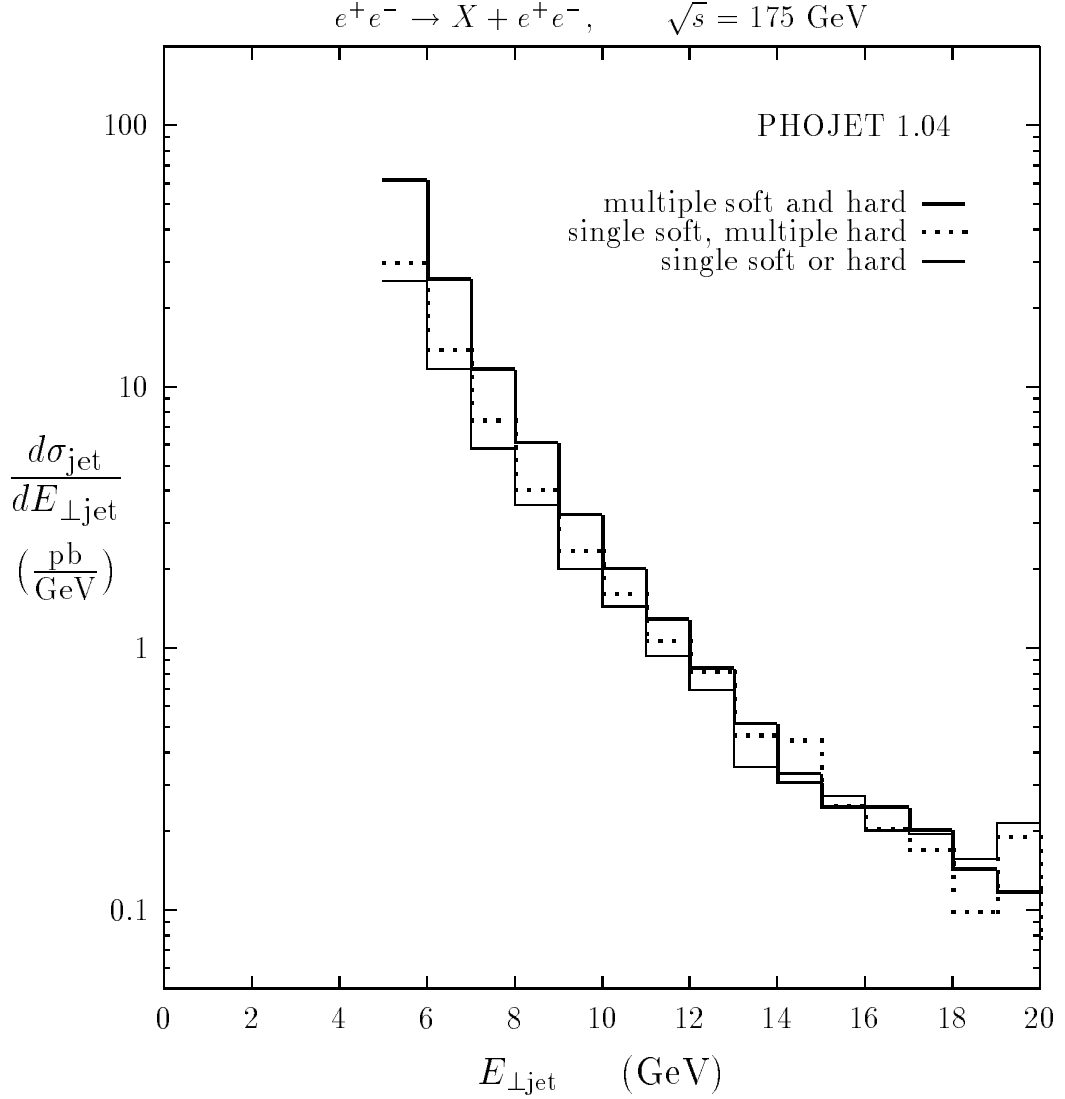


Figure 23: Jet cross section $d\sigma_{\text{jet}}/dE_{\perp\text{jet}}$ as function of the jet transverse energy. In order to study the influence of multiple soft and hard interactions in the model, we consider restricted cases with only single soft or single hard collisions. The curve with multiple soft, single hard collision coincides nearly with the full curve. The jets with $E_{\perp\text{jet}} \geq 5$ GeV were found from the PHOJET events using a cone algorithm. The jet acceptance region was restricted to $|\eta_{\text{jet}}| \leq 1.1$.

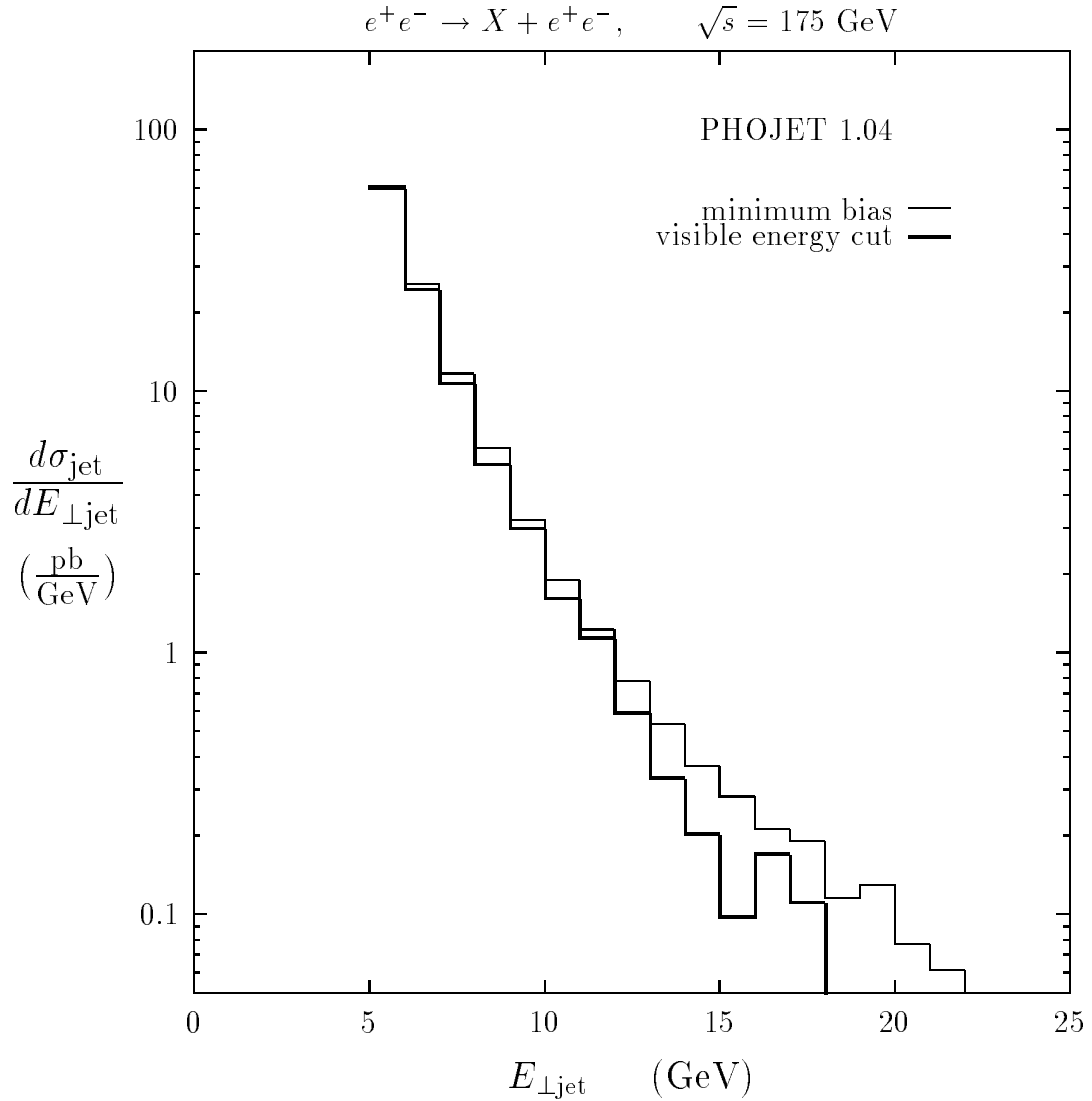


Figure 24: Jet cross section $d\sigma_{\text{jet}}/dE_{\perp\text{jet}}$ as function of the transverse energy. Here we give in addition the cross section with a visible energy cut (inside a calorimeter with $|\eta| \leq 2.1$ the cut is $E_{\text{visible}} \leq 50$ GeV). The jets with $E_{\perp\text{jet}} \geq 5$ GeV were found from the PHOJET events using a cone algorithm. The jet acceptance region was restricted to $|\eta_{\text{jet}}| \leq 1.1$.

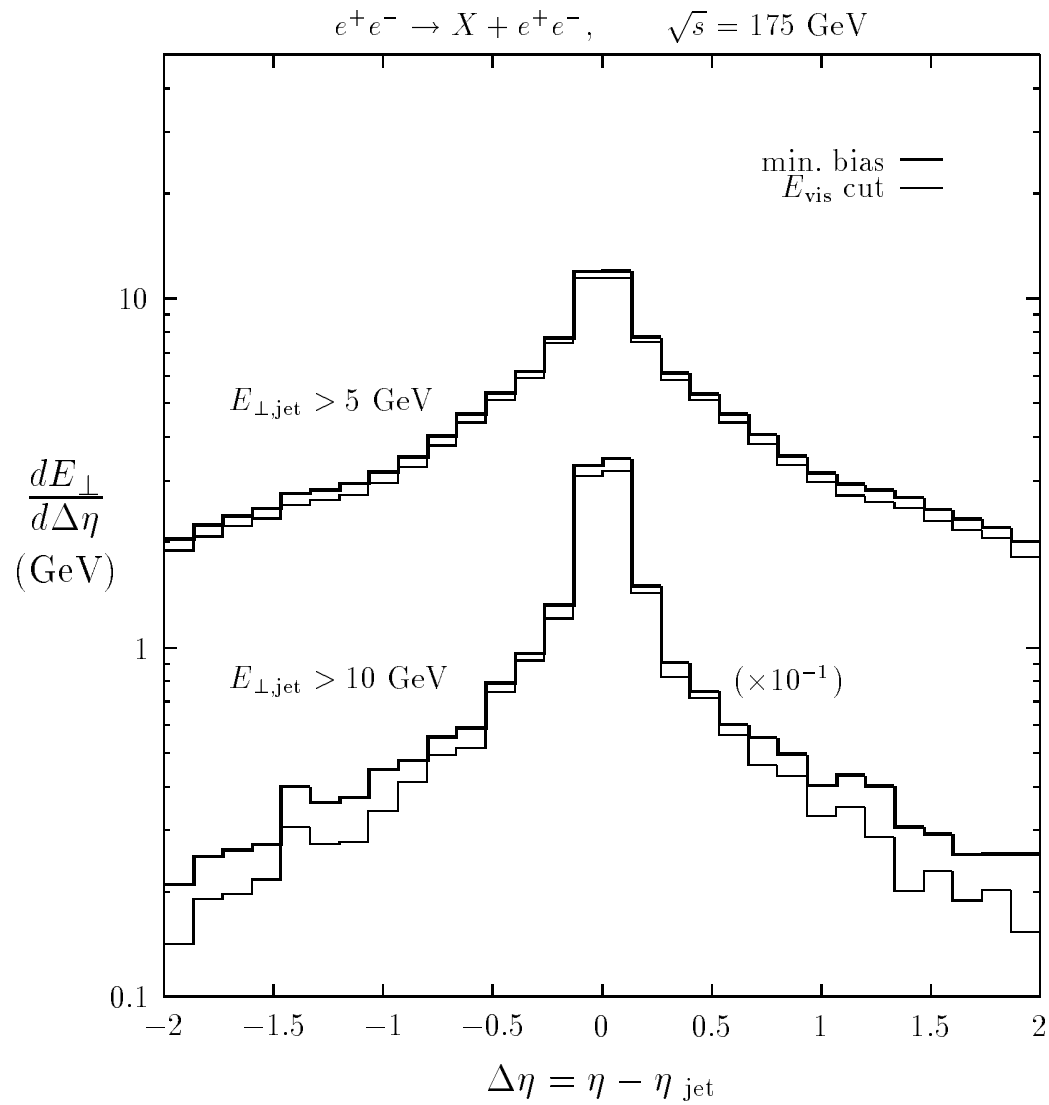


Figure 25: Jet profiles in the pseudorapidity variable with and without the visible energy cut described in the caption of Fig. 24.

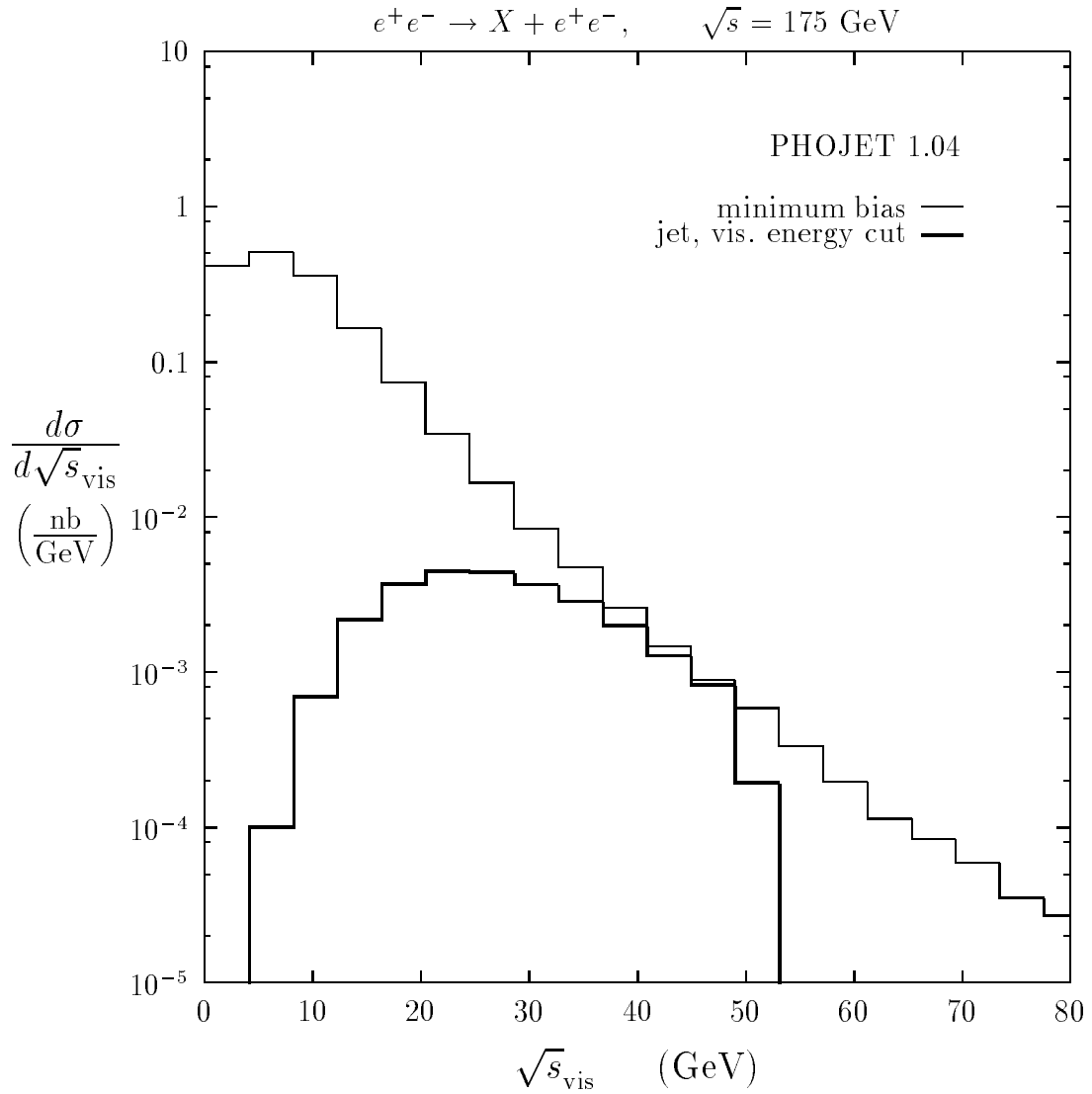


Figure 26: Cross section as function of the visible energy inside a calorimeter with $|\eta| \leq 2.1$. Only events with $\sqrt{s}_{\gamma\gamma} \geq 10$ GeV are sampled from the improved Weizsäcker-Williams spectrum. In a second curve we request jets with $E_{\perp\text{jet}} \geq 5$ GeV and impose a visible energy cut of 50 GeV.